nature energy

Article

https://doi.org/10.1038/s41560-023-01382-w

Polycrystalline silicon tunnelling recombination layers for high-efficiency perovskite/tunnel oxide passivating contact tandem solar cells

Received: 13 April 2023

Accepted: 22 September 2023

Published online: 9 November 2023

Check for updates

Jingming Zheng[1,4], Zhiqin Ying[1,4], Zhenhai Yang[1,2,4] ✉, Zedong Lin[3], He Wei[1], Li Chen[1], Xi Yang[1] ✉, Yuheng Zeng[1], Xiaofeng Li[2] ✉ & Jichun Ye[1] ✉

Perovskite/silicon tandem solar cells have rapidly advanced. Whereas efforts to enhance the device efficiency have mainly focused on top sub-cell improvements, the recombination layer connecting top and bottom sub-cells is critical for further progress. Here we present a perovskite/tunnel oxide passivating contact silicon tandem cell incorporating a tunnelling recombination layer composed of a boron- and phosphorus-doped polycrystalline silicon (poly-Si) stack. The poly-Si stack shows minimal interdiffusion of dopants. The strong adsorption ability of (2-(3,6-dimethoxy-9H-carbazol-9-yl)ethyl) phosphonic acid on poly-Si substrate enables efficient charge-carrier transport and extraction, particularly for the top perovskite sub-cells. The device achieves an efficiency of 29.2% (28.76% certified) and retains 85% of its initial efficiency after 500 hours of continuous maximum power point tracking. Additionally, we provide insights into the carrier transport and tunnelling mechanisms, offering guidance for the design of intermediate layers in the pursuit of high-efficiency tandem solar cells.

Tandem solar cells (TSCs) consisting of industrially matured crystalline silicon (c-Si) bottom cells and facile perovskite solar cells hold the potential to yield ultra-high efficiencies beyond the Shockley–Queisser limit of single-junction devices while maintaining cost advantages[1–5]. Through intensive worldwide efforts, the power conversion efficiency (PCE) of two-terminal perovskite/c-Si TSCs has increased from an initial 13.7% (ref. 6) to an impressive 33.7% (ref. 7) in recent years. To achieve this remarkable progress, extensive research on the top sub-cell has been conducted, resulting in excellent tandem-level results. This research has focused on various aspects, such as the regulation of perovskite composition/thickness, the introduction of additives or additional passivation layers and the development of suitable processes on textured c-Si substrates and so on[4,8–16]. However, it is important to note that further improvements in TSC efficiency require attention

[1]Zhejiang Provincial Engineering Research Center of Energy Optoelectronic Materials and Devices, Ningbo Institute of Materials Technology and Engineering, Chinese Academy of Sciences (CAS), Ningbo, China. [2]School of Optoelectronic Science and Engineering and Collaborative Innovation Center of Suzhou Nano Science and Technology; Key Lab of Advanced Optical Manufacturing Technologies of Jiangsu Province and Key Lab of Modern Optical Technologies of Education Ministry of China, Soochow University, Suzhou, China. [3]Guangdong Provincial Key Lab of Nano-Micro Materials Research, School of Chemical Biology and Biotechnology, Shenzhen Graduate School, Peking University, Shenzhen, China. [4]These authors contributed equally: Jingming Zheng, Zhiqin Ying, Zhenhai Yang. ✉e-mail: yangzhenhai@nimte.ac.cn; yangx@nimte.ac.cn; xfli@suda.edu.cn; jichun.ye@nimte.ac.cn

to critical functional layers, such as the ultrathin recombination layer (RL), which serves as an electrical contact connecting the top and bottom sub-cells[17].

A highly effective RL for TSCs should typically possess excellent optical properties with high infrared transparency to ensure sufficient optical absorption for the bottom sub-cell and good electrical performance to extract and recombine excess carriers from both the top and bottom sub-cells. To date, various strategies have been proposed to design RLs. Among them, transparent conductive oxides (TCOs), including indium tin oxide (ITO)[4], indium zinc oxide (IZO)[3], and aluminium-doped zinc oxide[18] and so on, have been widely employed as intermediate materials for high-efficiency TSCs. Through the regulation of the elemental component/proportion, thickness and deposition schedule, the photoelectrical properties of TCOs, including optical transparency, work function and electrical conductivity, can be tailored to construct TSCs with desired device performances. By completely removing the RLs, the RL-free TSCs rely on two polarity-opposite transport layers from the top and bottom sub-cells to create a p–n junction for carrier extraction and recombination, which can still operate but typically with lower efficiency (Supplementary Fig. 1 and Supplementary Table 1)[8,19]. Moreover, tunnelling recombination layer (TRL) based on nc-Si:H(p^+)/nc-Si:H(n^+) have also been widely employed to fabricate high-efficiency perovskite/c-Si TSCs[20,21]. Nonetheless, these designs have certain limitations as they may cause damage during film deposition or the thermal budget is limited to select the low-temperature process for top perovskite cells. A promising alternative is the polycrystalline silicon (poly-Si) stack consisting of poly-Si(p^+)/poly-Si(n^+), which is based on a tunnel oxide passivating contact (TOPCon) bottom sub-cell and can offer excellent passivation and contact properties simultaneously, therefore holding tremendous potential for use in perovskite/c-Si TSCs[22,23]. However, no relevant report exists to unlock this potential yet. Moreover, it is important to emphasize that perovskite/TOPCon TSCs are widely regarded as one of the most promising emerging technologies with industrialization potential for the next-generation photovoltaic (PV) industry, despite being in their infancy. The ever-increasing efficiency and the continuous reduction of manufacturing cost enables the fast adoption of TOPCon solar cells (SCs) as a mainstream technology since the year 2022 with a total capacity of over 400 GW at the end of 2023 as claimed by manufacturers[24]. Therefore, the further development of perovskite/TOPCon TSCs is of great significance for the PV industry.

Here we innovatively integrate a poly-Si(p^+)/poly-Si(n^+) tunnelling recombination layer (poly-Si TRL) into a high-efficiency perovskite/TOPCon TSC. By intrinsically suppressing dopant interdiffusion and compensation, we achieve a high-quality poly-Si TRL with excellent passivation performance and low contact resistance. Density functional theory (DFT) calculations, combined with experiment results, reveal that the (2-(3,6-dimethoxy-9H-carbazol-9-yl)ethyl) phosphonic acid (MeO-2PACz) hole transport layer (HTL) is more readily adsorbed onto the SiO_2-based poly-Si(p^+) than the normal IZO substrate. As a consequence, the TSCs with poly-Si TRL exhibit enhanced charge-carrier transport and extraction, especially for the top perovskite sub-cells. Additionally, we comprehensively investigate carrier transport and tunnelling mechanisms of this type of TSCs through detailed finite element simulations. The resulting perovskite/TOPCon TSC with poly-Si TRL achieves a remarkable efficiency of 29.2% and great stability, retaining 85% of its initial PCE after 500 hours of continuous maximum power point (MPP) tracking.

Photovoltaic performance of perovskite/TOPCon TSCs

Figure 1a illustrates the structural diagram of the perovskite/TOPCon TSC with poly-Si TRL. In this study, the front and rear surfaces of c-Si were textured by black silicon (b-Si) (with a feature size of ~200 nm) and random pyramid (with a feature size of several microns) structures, respectively. The composition and crystal structure of the poly-Si(p^+)/poly-Si(n^+) stack were explored using high-resolution scanning transmission electron microscopy (HR-TEM) and energy dispersive spectrometer (EDS) mappings as displayed in Fig. 1b (planar surface) and Supplementary Fig. 2 (b-Si surface). Upon careful observation, several key findings emerged: (1) the typical single crystal diffraction patterns for the perovskite and c-Si within the selected regions can be seen, which are the signal of high-quality perovskite film and c-Si substrate; (2) the obvious polycrystalline feature concluded from the diffraction pattern of poly-Si (region II), together with the appearance of polycrystalline phases in many local regions, indicates a high crystallinity of poly-Si film; (3) the thickness of poly-Si including poly-Si(p^+) and poly-Si(n^+) is determined to be ~31 nm (as confirmed by scanning electron microscope (SEM) images in Supplementary Fig. 3), and an intact SiO_x with a uniform thickness of ~1.7 nm can be observed, implying high-quality chemical passivation by SiO_x; (4) no significant grain boundary regionalization or boundary existence was observed at the poly-Si(p^+)/poly-Si(n^+) interface within region II as shown in Fig. 1b. EDS mapping and distribution of the P element, as demonstrated in Supplementary Fig. 4, clearly show a steep transition between the poly-Si(n^+) and poly-Si(p^+) regions.

The PV performance of perovskite/TOPCon TSCs with poly-Si TRL was then investigated, in which the counterpart with the normal IZO RL was also shown as a comparison. The device fabrication details are summarized in the Methods section. In addition, the thickness of the perovskite layer, as confirmed by SEM images in Supplementary Fig. 3, is approximately 550 nm. This thickness is notably different from the submicrometric pyramid textures, which typically require a much thicker perovskite layer (>1 μm) to achieve full coverage. Figure 1c demonstrates the current density–voltage (*J*–*V*) curves of the two relevant TSCs with the best device efficiencies. The TSC with poly-Si TRL exhibits a higher PCE of 29.2% with an open-circuit voltage (V_{oc}) of 1.83 V, a J_{sc} of 19.7 mA cm^{-2} and a fill factor (FF) of 81.0%, which is slightly higher than that of the IZO RL counterpart (28.5%) with a V_{oc} of 1.76 V, a J_{sc} of 19.8 mA cm^{-2} and an FF of 81.9%. It is worth noting that, to the best of our knowledge, the efficiency of 29.2% demonstrated in this study is among the highest for the perovskite/TOPCon TSCs so far (Supplementary Fig. 5 and Supplementary Table 1). Figure 1d compares the statistics of the PCE values of perovskite/TOPCon TSCs with IZO RL and poly-Si TRL. The results indicate that the average PCEs for TSCs with IZO RL and poly-Si TRL were determined to be 28.3% and 28.9%, respectively. Additionally, the corresponding V_{oc},J_{sc} and FF statistics presented in Fig. 1d and Supplementary Figs. 6 and 7 suggest that the enhanced efficiency observed in poly-Si TRL-based TSCs can be primarily attributed to the improved V_{oc} when compared with that of IZO RL-based TSCs. Figure 1e plots the corresponding external quantum efficiency (EQE) spectra of the two related sub-cells, with the integral current densities consistent with that of the *J*–*V* results. Figure 1f illustrates the certified *J*–*V* curve of TSC with poly-Si TRL (an active area of 0.1321 cm^2), which receives a remarkable PCE of 28.76% (certified report in Supplementary Fig. 8). Moreover, the long-term stability of the relevant devices was also studied as shown in Fig. 1g. For MPP tracking under continuous xenon-lamp illumination without filtering ultraviolet in the air (relative humidity (RH) = 40–70%, temperature (*T*) = 20–35 °C), the simple-encapsulated TSC with poly-Si TRL exhibited promising long-term stability, retaining 85% of its initial PCE after 500 hours. This performance surpasses that of the IZO counterpart, indicating that the poly-Si TRL also contributes to improved device stability.

Characterization of poly-Si tunnelling junction

It has been confirmed by a large body of evidence that restraining parasitic dopant interdiffusion between poly-Si(p^+) and poly-Si(n^+) layers is the key to obtaining high-quality poly-Si(p^+)/poly-Si(n^+) tunnelling junction (TJ)[13,14]. To evaluate the properties of poly-Si(p^+)/poly-Si(n^+) TJ, electrochemical capacitance voltage (ECV) and secondary ion mass

https://doi.org/10.1038/s41560-023-01382-w

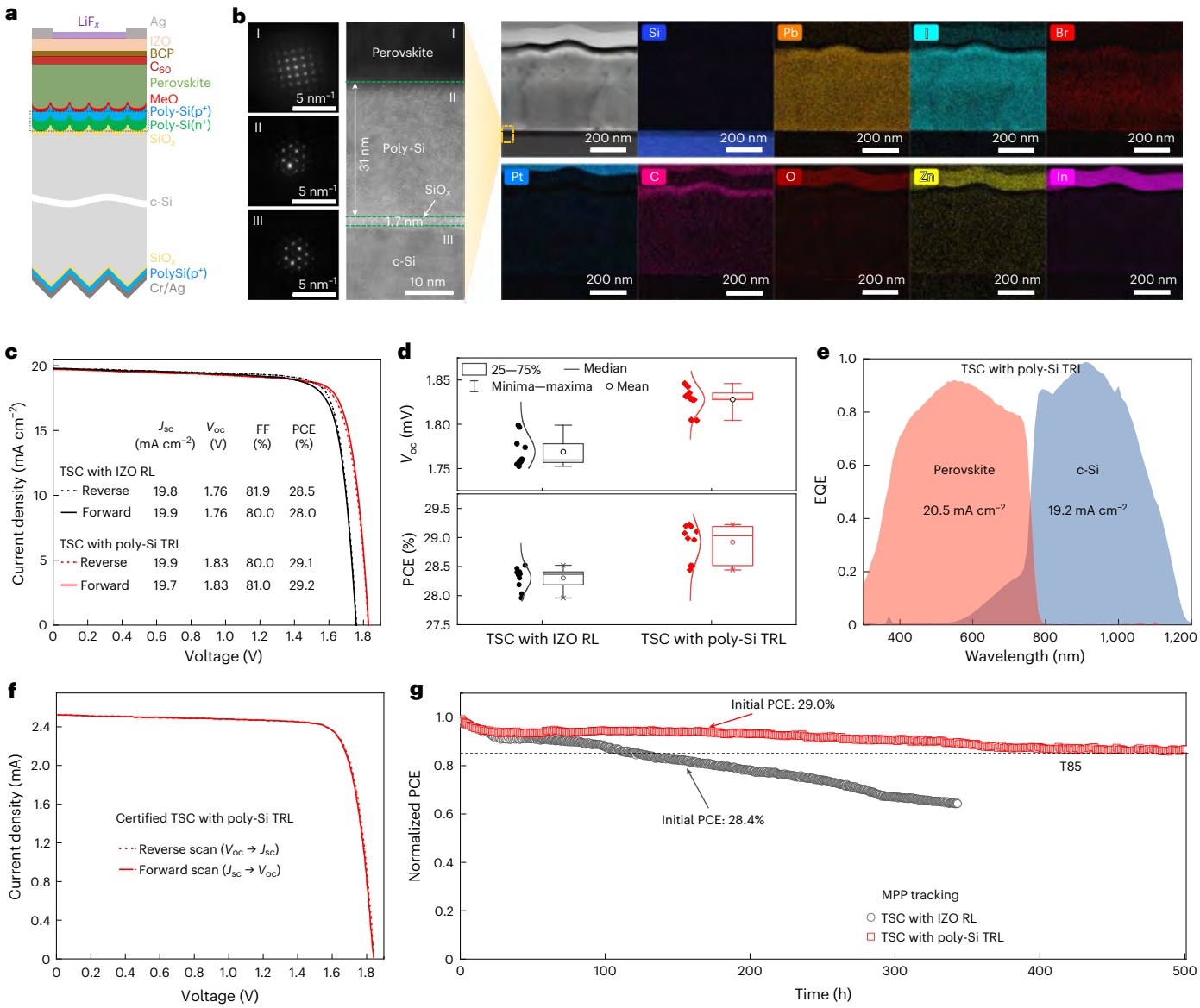

Fig. 1 | Microscopic and photovoltaic properties. a, Structural diagram of perovskite/TOPCon TSC with poly-Si TRL. **b**, HR-TEM image and the corresponding nanobeam diffraction patterns measured on perovskite, poly-Si and n-type silicon (n-Si) substrate regions under scanning transmission electron microscopy mode and EDS mappings (including Si, Pb, I, Br, Pt, C, O, Zn and In elements). **c**, (*J*–*V*) curves of perovskite/TOPCon TSCs with IZO RL and poly-Si TRL (with an aperture area of 0.1 cm^2), where the corresponding electrical parameters are tabled in the inset. **d**, Statistical distribution along with the fits (normal distribution of data points) of the V_{oc} and PCE values of perovskite/TOPCon TSCs with IZO RL and poly-Si TRL. The lines, arranged from top to bottom, represent the maximum, upper quartile (upper edge of the box), median, lower quartile (lower edge of the box) and minimum values within the dataset. Each experimental condition comprised ten individual samples. **e**, EQE spectra of the two related TSCs, in which the integrated photogenerated current densities of each sub-cell are demonstrated. **f**, Certified *J*–*V* curve of perovskite/TOPCon TSC with poly-Si TRL (0.1321 cm^2). **g**, Long-term MPP tracking under continuous xenon-lamp illumination without filtering ultraviolet in the air (RH = 40–70%, *T* = 20–35 °C) for simple-encapsulated TSCs with IZO RL and poly-Si TRL, where the initial *I*–*V* curves of the two related TSCs were demonstrated in Supplementary Fig. 9. Considering the measurement noise, the data are normalized to the MPP average of the first ten hours of each track. The initial efficiencies of stability testing for TSCs with IZO RL and poly-Si TRL are 28.4% and 29.0%, respectively.

spectrometry (SIMS) measurements were conducted to quantify the activated and dopant impurities (that is, B or P). As illustrated in Fig. 2a,b, the concentration of activated/doped B (P) impurity within the poly-Si(p$^+$) (poly-Si(n$^+$)) layer remains relatively high and displays a sharp dopant boundary at the poly-Si(p$^+$)/poly-Si(n$^+$) interface, suggesting limited dopant compensation and interdiffusion. To further support this conclusion, the activated B/P concentration profiles of the TJ-free sample from ECV measurement, together with H and O concentration profiles from SIMS measurement, were also checked, as shown in Supplementary Figs. 10 and 11, respectively. Additionally, the energy band diagram of such a TJ was simulated based on the activated B and P concentration profiles from Fig. 2a, with the corresponding results demonstrated in Fig. 2c. It is apparent that the valence band of poly-Si(p$^+$) and conduction band of poly-Si(n$^+$) exhibit an energy overlap, combined with a narrow depletion width (~6 nm), implying the formation of a highly efficient TJ.

To further evaluate the quality of poly-Si(p$^+$)/poly-Si(n$^+$) TJ, we investigated the passivation and contact properties of samples with this type of TJ. Figure 2d depicts the implied open circuit voltage (iV_{oc}) curves of samples with TJ structures, that is, poly-Si(p$^+$)/poly-Si(n$^+$)/n-Si/poly-Si(n$^+$) and poly-Si(p$^+$)/poly-Si(n$^+$)/n-Si/poly-Si(p$^+$), which are almost identical to those of TJ-free counterparts, that is,

https://doi.org/10.1038/s41560-023-01382-w

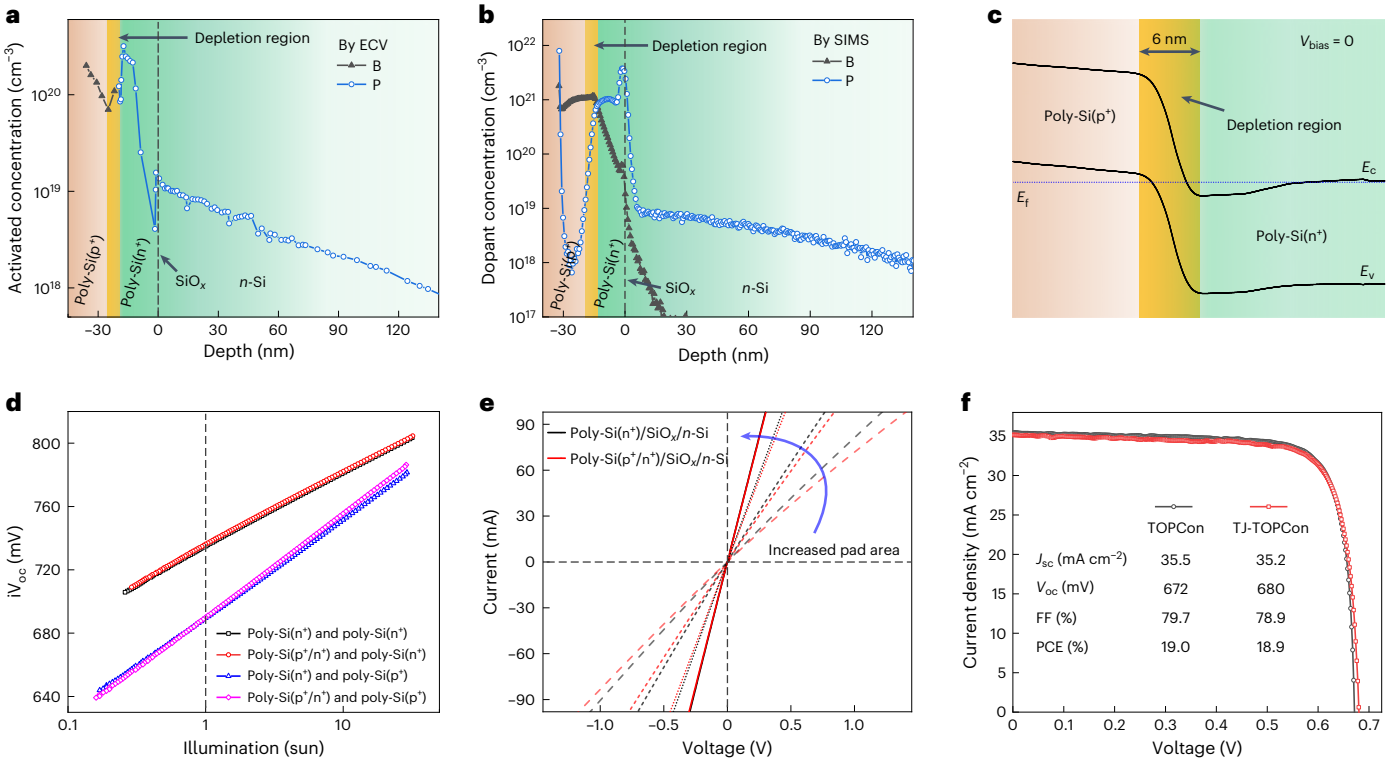

Fig. 2 | Characteristics and performance. a,**b**, Activated and dopant B and P concentration profiles of poly-Si(p$^+$)/poly-Si(n$^+$)/SiO$_x$/n-Si structures measured by ECV (**a**) and by SIMS (**b**). **c**, Calculated energy band diagram of poly-Si(p$^+$)/poly-Si(n$^+$) TJ under V_{bias} = 0, where the doping concentrations of poly-Si(p$^+$) and poly-Si(n$^+$) layers were extracted from the ECV curve. Here the background colours of red, yellow, and green in **a**–**c** correspond to the B-doping, depletion and P-doping regions, respectively, and the intensity of the colour qualitatively illustrates the strength of the doping concentration. E_c, E_v and E_f represent the bottom of the conduction band, the top of the valence band and Fermi energy, respectively. **d**, Illumination intensity-dependent iV$_{oc}$ curves for the different samples, that is, poly-Si(n$^+$)/SiO$_x$/n-Si/SiO$_x$/poly-Si(n$^+$), poly-Si(p$^+$)/poly-Si(n$^+$)/SiO$_x$/n-Si/SiO$_x$/poly-Si(n$^+$), poly-Si(n$^+$)/SiO$_x$/n-Si/SiO$_x$/poly-Si(p$^+$) and poly-Si(p$^+$)/poly-Si(n$^+$)/SiO$_x$/n-Si/SiO$_x$/poly-Si(p$^+$). **e**, Dark *I*–*V* curves of samples with poly-Si(n$^+$)/SiO$_x$/n-Si and poly-Si(p$^+$)/poly-Si(n$^+$)/SiO$_x$/n-Si structures measured on metal pads with various areas. **f**, Light *J*–*V* characteristics of TOPCon and TJ-TOPCon SCs along with the corresponding electrical parameters (refer to Supplementary Fig. 10 for the corresponding schematic diagrams).

poly-Si(n$^+$)/n-Si/poly-Si(n$^+$) and poly-Si(n$^+$)/n-Si/poly-Si(p$^+$). This implies that introducing an additional poly-Si(p$^+$) layer on top of the poly-Si(n$^+$) layer will not degrade the passivation quality of samples. Moreover, effective minority carrier lifetime (τ_{eff}) curves (Supplementary Fig. 12 and Supplementary Table 2) and photoluminescence (PL) images (Supplementary Fig. 13) were also presented to confirm this conclusion. Figure 2e illustrates the typical current–voltage (*I*–*V*) curves used to evaluate the contact property, revealing that the TJ sample, especially for cases with smaller pad areas, shows slightly higher contact resistivity compared with the TJ-free sample. Nevertheless, all plots maintain linear *I*–*V* characteristics, which is a sign of Ohmic behaviour, suggesting that the presence of TJ will not significantly deteriorate the contact performance. To further confirm the feasibility of this type of TJ design, the completed c-Si SCs with poly-Si(p$^+$)/poly-Si(n$^+$) TJ structure were fabricated (Supplementary Fig. 14). The typical *J*–*V* characteristics and the corresponding electrical parameters are illustrated in Fig. 2f. From this figure, it is evident that TJ-TOPCon has a distinct advantage in V_{oc} compared to TJ-free TOPCon (Supplementary Fig. 15), with a V_{oc} enhancement of 8 mV (that is, from 672 mV of TJ-free TOPCon to 680 mV of TJ-TOPCon). This improvement in V_{oc} can be primarily attributed to the prevention of sputtering damage caused by ITO deposition during the physical vapour deposition process. The validity of the V_{oc} enhancement due to the TJ design is further supported by capacitance–voltage (*C*–*V*) measurement, which suggests a built-in voltage of 764 and 775 mV for the TOPCon and TJ-TOPCon SCs, respectively (Supplementary Fig. 16). Although TJ-TOPCon SCs demonstrate a slightly lower FF (78.9%) than that of TJ-free device (79.7%) due to a mild increase in contact resistance, this has been confirmed to have less effect on perovskite/TOPCon TSCs[25]. Additionally, TJ-TOPCon SCs exhibit a slightly lower J_{sc} (that is, 35.5 and 35.2 mA cm^{-2} for TJ-free TOPCon and TJ-TOPCon, respectively) owing to the differences in optical management (Supplementary Figs. 17 and 18), which, however, can be compensated in TSCs. As a result, the efficiencies of TJ-free TOPCon and TJ-TOPCon are determined to be 19.0% and 18.9%, respectively. Considering the multitude of parameters that can affect device efficiency, the observed differences in electrical performance may not provide conclusive evidence regarding the specific impact of different designs on overall device performance. However, it is crucial to highlight that the introduction of poly-Si(p$^+$)/poly-Si(n$^+$) TJ will not have a detrimental effect on the performance of the TOPCon SCs.

Calculation and characteristics of MeO-2PACz adsorption

As the MeO-2PACz is an ultrathin self-assembled organic monolayer, which is a common HTL used for the perovskite sub-cell, controlling the amount of MeO-2PACz adsorption on the intermediate layers is thus extremely crucial for the perovskite/TOPCon TSCs. To improve the surface wettability of poly-Si, we conducted ozone treatment on the sample before depositing MeO-2PACz, which led to the formation of an extremely thin layer of SiO_2. Therefore, when performing calculations for the adsorption of MeO-2PACz, we consider an ultrathin SiO_2 for the poly-Si sample. To investigate the adsorption ability of MeO-2PACz on the IZO and SiO_2-based poly-Si substrates, we conducted a first-principles DFT simulation, as demonstrated in Fig. 3a,b. Here

https://doi.org/10.1038/s41560-023-01382-w

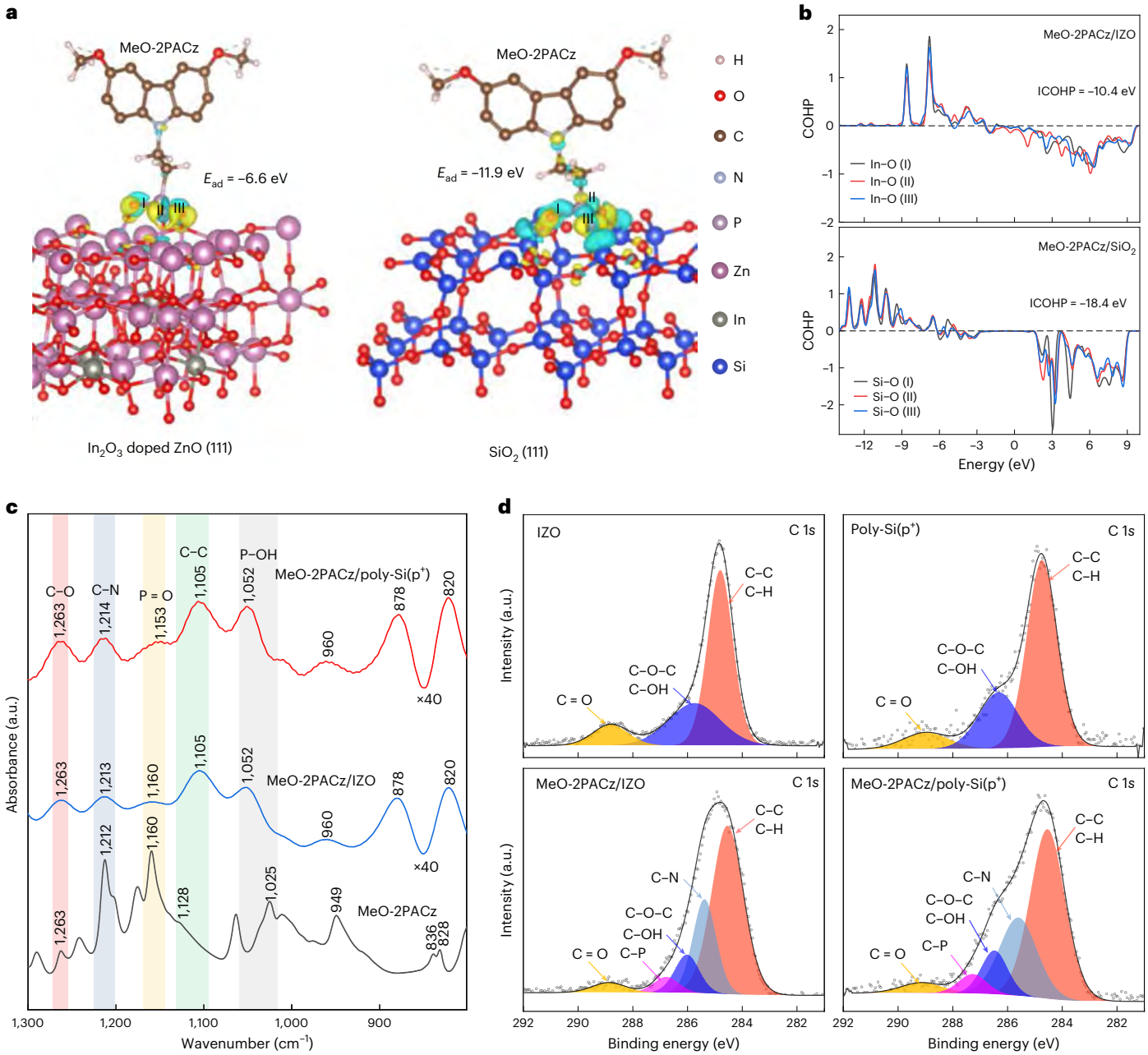

Fig. 3 | MeO-2PACz adsorption calculation and characteristics. a,**b**, Local charge density distributions of MeO-2PACz adsorbed IZO (111) and SiO_2 (111)-based poly-Si substrates (**a**) and the corresponding COHP curves (**b**). The cyan and yellow volumes correspond to electron-depleted or electron-enriched regions, respectively. The numerals I, II and III indicate the number of bonds. **c**, FTIR absorbance spectra of MeO-2PACz coated IZO and poly-Si(p^+) samples, where the sample of bulk MeO-2PACz in the KBr tablet was also presented as a reference. **d**, XPS spectra of C 1*s* region of samples with IZO, poly-Si(p^+) and MeO-2PACz coated IZO and poly-Si(p^+) substrates. XPS peaks were fitted using Gaussian peak fitting.

the cyan cloud indicates the electron loss from the relative bonds or atoms after charge redistribution, and the yellow cloud denotes the electrons trapped by the relative atoms[26]. The charge transfer between the surface I/II/III of IZO (or SiO_2-based poly-Si) and MeO-2PACz occurs by forming In–O (or Si–O) bonds, indicating a strong interaction between IZO (or SiO_2-based poly-Si) and MeO-2PACz. Moreover, the DFT simulation results suggest the adsorption energies (E_{ad}) of MeO-2PACz on IZO and SiO_2-based poly-Si substrates are −6.6 and −11.9 eV, respectively, implying a stronger adsorption ability of MeO-2PACz on the SiO_2-based poly-Si substrate[27]. We further calculated the crystal orbital Hamilton population (COHP) to represent the strength of chemical bonds, as displayed in Fig. 3b. In particular, the total energy integral COHP (ICOHP) for IZO (SiO_2-based poly-Si) substrate is determined to be −10.4 (−18.4) eV (Supplementary Table 3), indicating that MeO-2PACz forms more stable and strong chemical bonds when adsorbed on the SiO_2-based poly-Si substrate[28]. Furthermore, we also took into account the adsorption of MeO-2PACz on other crystal surfaces of the substrates, as depicted in Supplementary Figs. 19 and 20. These findings consistently indicate that MeO-2PACz exhibits stronger adsorption capability on SiO_2-based poly-Si substrate, regardless of the specific crystal planes involved.

In addition, Fourier transform infrared spectrometer (FTIR) measurement was performed to explore the bonding configuration of MeO-2PACz and its interaction with IZO and poly-Si(p^+) substrates. As

can be seen from Fig. 3c (Supplementary Fig. 21), the bulk MeO-2PACz shows three characteristic FTIR peaks owing to carbazole stretching at 828, 836 and 949 cm^{-1}, which shifted to 820, 878 and 960 cm^{-1} for the two related samples[29]. Moreover, the four FTIR peaks at 1,160; 1,128; 1,212 and 1,263 cm^{-1} for the bulk MeO-2PACz were assigned to P=O, C–C, C–N and C–O stretching vibrations[30], respectively, which were also observed in our studied samples, indicating the bonding of MeO-2PACz on the IZO and poly-Si(p^+) surfaces. The C–C stretching peak at 1,128 cm^{-1} for the bulk MeO-2PACz shifted to 1,105 cm^{-1} for the two studied samples due to the differences in the flexibility of large groups or group chains in bulk materials and thin films[31]. Notably, a 7 cm^{-1} shift of the P=O peak, which is prominent in the bulk MeO-2PACz at 1,160 cm^{-1}, can be seen, possibly due to the different adsorption sites between IZO and poly-Si(p^+). Additionally, the disappearance of the P–OH peak at 1,025 cm^{-1} for the bulk MeO-2PACz, together with the appearance of the characteristic peak at 1,052 cm^{-1} for the two studied samples, suggests that the P–OH bonds lose H and combine with IZO and poly-Si(p^+) to form P–O–Zn and P–O–Si, confirming the adsorption of MeO-2PACz on IZO and poly-Si(p^+) substrates[32].

To gain insights into the chemical states of the MeO-2PACz coated IZO and poly-Si(p^+) samples, XPS measurements were carried out with the corresponding results shown in Fig. 3d. The C 1*s* XPS spectra for the IZO sample were decomposed into three components contributed by C–C/C–H (284.9 eV), C–O–C/C–OH (285.7 eV) and C=O (288.8 eV) (ref. 33). By coating the MeO-2PACz on top of IZO, two additional peak components that belong to C–N (285.4 eV) and C–P (286.8 eV) (ref. 33) appeared, signifying the bonding configuration of MeO-2PACz on the IZO substrate. A similar phenomenon was obtained in the MeO-2PACz coated poly-Si(p^+) sample. Additionally, N 1*s*, O 1*s*[32], In 3*d*[30] and Si 2*p* signs were also observed to confirm the successful adsorption of MeO-2PACz on the two related substrates (Supplementary Figs. 22–24). Furthermore, compared with the MeO-2PACz/IZO, the MeO-2PACz coated poly-Si(p^+) showed stronger C–N and C–P peaks and higher N and P contents calculated by the area of these characteristic peaks (Supplementary Table 4), indicating a stronger adsorption of MeO-2PACz on poly-Si(p^+) substrate.

Characteristics of carrier extraction

In this section, the electrical properties related to the energy band structure and charge-carrier transport/extraction behaviour is checked. First of all, Kelvin probe force microscopy (KPFM) measurements were performed to verify the surface potential distributions. Figure 4a displays the three-dimensional KPFM maps, which indicates average potentials of 414, 337, 101 and 68 mV for the poly-Si(p^+), IZO and MeO-2PACz coated IZO and poly-Si(p^+) surfaces, respectively (Supplementary Fig. 25). It is widely accepted that a lower surface potential signifies a higher work function or Fermi level, which is beneficial to forming a favourable energy-level alignment between perovskite and HTL to promote the extraction of holes. Therefore, based on the energy band structure and carrier extraction viewpoint, poly-Si(p^+) is the better RL for the TSC. To further support this conclusion, ultraviolet photoelectron spectroscopy (UPS) measurements were conducted. Figure 4b shows that the work functions of the poly-Si(p^+), IZO and MeO-2PACz coated IZO and poly-Si(p^+) surfaces were determined to be 4.11, 4.21, 4.43 and 4.58 eV, respectively, which is consistent with the KPFM results.

To further comprehend the beneficial impact of poly-Si(p^+) on the top perovskite sub-cells, the steady-state photoluminescence (PL) and time-resolved PL (trPL) measurements were carried out with the corresponding results illustrated in Fig. 4c,d, respectively. The steady-state PL spectrum of perovskite film deposited on MeO-2PACz/poly-Si(p^+) substrate in Fig. 4c (red line) exhibits obvious intensity quenching compared to that of perovskite film on MeO-2PACz/IZO substrate (black line). The trPL decay demonstrated in Fig. 4d suggests a fast/long/average lifetime ($\tau_1/\tau_2/\tau_{ave}$) of 36.2/737.4/719.7 and 12.1/692.9/672.0 ns for the PSK/MeO-2PACz/IZO and PSK/MeO-2PACz/poly-Si(p^+) samples, respectively (Supplementary Fig. 29 and Table 5). The steady-state PL and trPL results indicate a significant enhancement in carrier extraction for the PSK/MeO-2PACz/poly-Si(p^+) samples[34].

To gain a deeper insight into the charge recombination dynamics, we carried out ultrafast transient absorption (fs-TA) characterization. Figure 4e,f displays the pseudocolour fs-TA plots of two related samples, where a broad photoinduced absorption (absorption change intensity: $\Delta A > 0$) signal and a clear photobleaching (PB, $\Delta A < 0$) signal were detected[35]. To facilitate observation and comparison, we depicted the time evolution fs-TA plots concerning the main features of samples in Fig. 4g,h. The PB signals near the band edge region, which is correlated with the population of excited charges, contribute to the analysis of charge transfer and recombination kinetics of the perovskite films, as we emphasize in this study. The initial evolution of the PB signals within 2 ps is identical for the two related samples due to the Wannier–Mott type excitons of perovskite with low binding energy. The PB peaks rapidly intensify within 10 ps due to hot carrier cooling. After that, the time-dependent PB peaks (solid lines) can be attributed to the bimolecular recombination within a few hundred picoseconds, whereas the long-time PB signals (that is, thousands of picoseconds) should be related to the trap-assisted monomolecular recombination[36]. In addition, the normalized decay kinetic curves at 735 nm extracted from the fs-TA spectra were well-fitted by a bi-exponential function as shown in Fig. 4i. As a result, the poly-Si(p^+) sample receives a lower fast lifetime of 189.4 ns compared to the IZO sample of 275.8 ns, suggesting a promoted extraction of holes and an effective suppression of non-radiative recombination at the perovskite/HTL interface. On the basis of the aforementioned results, it can be inferred that the improvement in V_{oc} and PCE of the poly-Si TRL-based TSCs is primarily attributed to the perovskite-based top sub-cell, while the V_{oc} contribution from the bottom sub-cell is relatively small (less than 10 mV). This outcome can be attributed to the stronger MeO-2PACz adsorption and higher substrate work function in the perovskite-based top sub-cell. The improved carrier transport and extraction observed in poly-Si TRL-based TSCs, in contrast to IZO RL-based TSCs, represent the primary factors driving the enhancement of V_{oc} and PCE of poly-Si TRL-based TSCs.

Carrier transport and tunnelling mechanisms

In this section, we will study the carrier transport and tunnelling mechanisms of perovskite/TOPCon TSCs with poly-Si TRL. The device simulation was conducted using the finite element method within the Silvaco TCAD software. The energy band diagram of such a device is illustrated in Fig. 5a, which is consistent with the configuration of our experiment. The profiles of the hole and electron current densities (that is, J_h and J_e) within the devices under short circuit (SC), open circuit (OC) and MPP conditions are presented in Fig. 5b. At the SC condition, an increase in J_e from ETL to HTL within the perovskite layer (solid blue line), along with a reversed J_h within the c-Si layer (solid red line), leads to a higher current output. Moreover, a high J_h at the rear side of the perovskite sub-cell and a high J_e at the top side of the c-Si sub-cell are observed, which disappear within poly-Si TRL. For the MPP condition, similar trends but with slightly reduced response currents (compared with the SC condition) can be found. As for the OC condition, symmetrical J_h and J_e distributions within the perovskite and c-Si sub-cells can be observed, meaning that carriers within the devices are completely recombined with a net current of zero.

To further illustrate the carrier recombination behaviours of poly-Si TRL, J_h and J_e profiles, along with the corresponding energy diagrams within the poly-Si(p^+) and poly-Si(n^+) regions at MPP were presented in Fig. 5c,d, where two typical doping concentrations (N_d), that is, $N_d = 2 \times 10^{19}$ and 10^{20} cm^{-3}, are considered. As displayed in Fig. 5c, an intersecting falloff in current, together with a high recombination rate within the depletion region for $N_d = 2 \times 10^{19}$ cm^{-3} can be seen, which is a signal of carrier recombination in the depletion region. Moreover, the corresponding energy diagram shows that the Fermi energy levels

https://doi.org/10.1038/s41560-023-01382-w

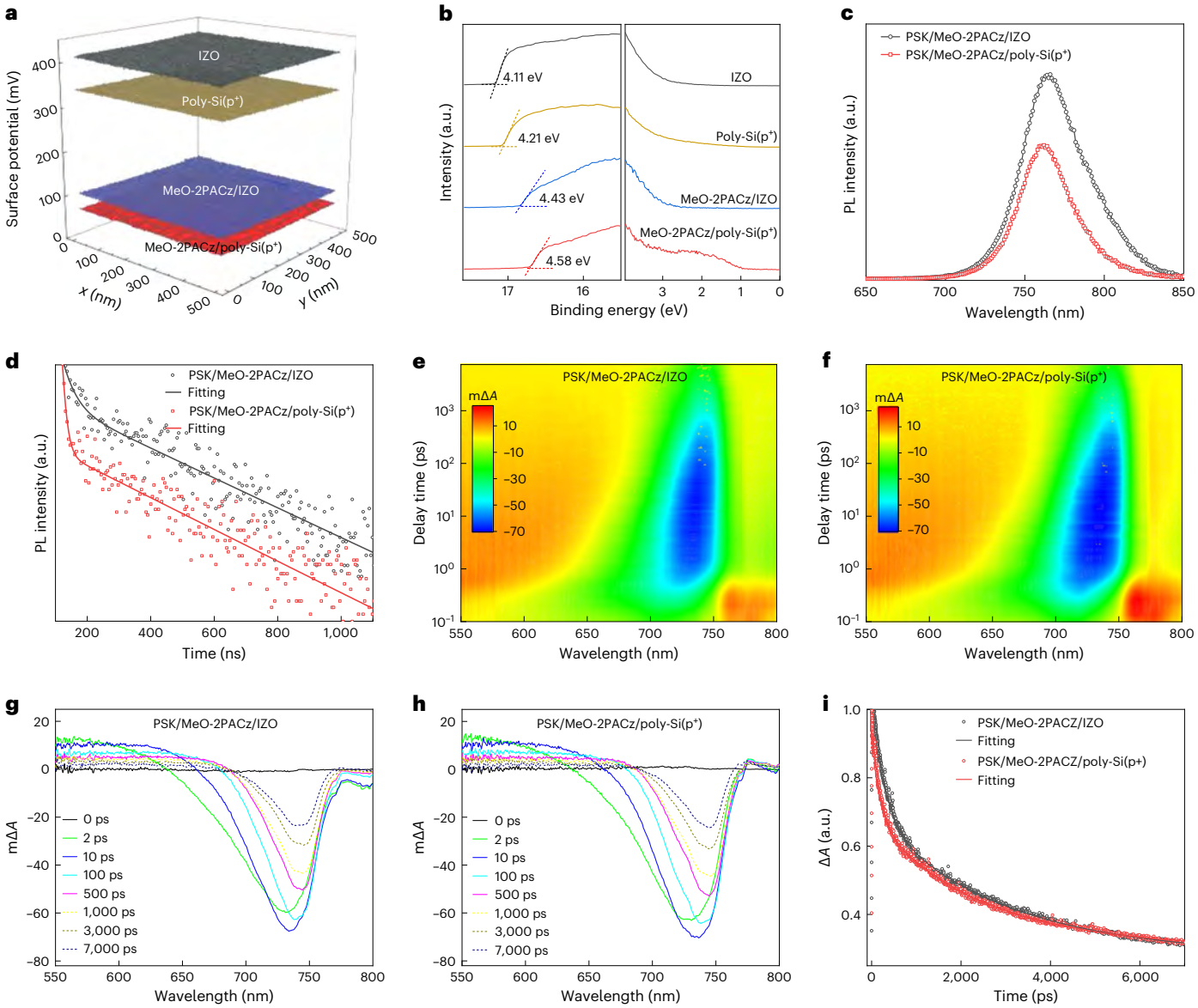

Fig. 4 | Electrical characteristics of samples on IZO and poly-Si(p$^+$) substrates. **a**,**b**, Three-dimensional KPFM maps (**a**) and UPS spectra (**b**) of four related samples, that is, IZO, poly-Si(p$^+$), MeO-2PACz/IZO and MeO-2PACz/poly-Si(p$^+$). **c**,**d**, Steady-state (**c**) and time-resolved PL (**d**) spectra. A bi-exponential function was employed to fit the trPL curves in **d**. **e**–**h**, Pseudocolour fs-TA plots as functions of wavelength and probe delay time for the perovskite films deposited on MeO-2PACz/IZO (**e**) and MeO-2PACz/polySi(p$^+$) (**f**) substrates, where the colour scale bar stands for the absorption change intensity (ΔA), and fs-TA plots of milli ΔA (mΔA) under the different probe delay times excited at 450 nm for the perovskite films deposited on MeO-2PACz/IZO (**g**) and MeO-2PACz/poly-Si(p$^+$) (**h**) substrates. **i**, Normalized decay kinetic curves at 735 nm extracted from the fs-TA spectra. A bi-exponential function was employed to fit the plots. Here we performed multiple UPS, PL and trPL measurements to ensure the reliability of the results. The corresponding data of duplicate testing are provided in Supplementary Figs. 26–28, demonstrating consistent outcomes. These findings affirm the credibility of the tests conducted. In this context, it is worth noting that the *y*-axes of **b** and **c** employ a linear scale, while **d** utilizes a logarithmic scale.

of poly-Si(p$^+$) and poly-Si(n$^+$) are clearly separated and the valence band of poly-Si(p$^+$) and conduction band of poly-Si(n$^+$) show no energy overlap. These observations, combined with the thick depletion layer (~14 nm), suggest that carriers are more likely to be recombined by means of trap-assisted tunnelling (TAT) rather than band-to-band tunnelling (BBT)[37]. For the case of $N_d = 10^{20}$ cm^{-3} as displayed in Fig. 5d, the depletion region is reduced to ~7 nm (Supplementary Fig. 30), and an obvious energy overlap between poly-Si(p$^+$) and poly-Si(n$^+$) is obtained, indicating that carrier transport is dominated by BBT. Additionally, a high BBT recombination rate (that is, $R_{BBT\text{-}e}$ and $R_{BBT\text{-}h}$) together with the appearance of a forbidden region of carrier recombination within the depletion region can be observed, which verifies that carrier transport and recombination mechanisms are dominated by BBT behaviour if poly-Si is highly doped. Furthermore, samples under SC and OC conditions are also presented in Supplementary Fig. 31.

The impact of the doping concentration of poly-Si(p$^+$) and poly-Si(n$^+$) on device performance was investigated with the corresponding results demonstrated in Fig. 5e. To strictly distinguish the inherent correlation of two related transport mechanisms (that is, TAT and BBT) and device performance, we consider three simulation models, that is, TAT without BBT, BBT without TAT and TAT coupled BBT. If we only consider the TAT model, V_{oc} and J_{sc} for all defect concentration (N_t) cases (blue lines) show an increasing trend with the increase of N_d from 10^{19} to 4×10^{20} cm^{-3}, but FF and PCE show an

https://doi.org/10.1038/s41560-023-01382-w

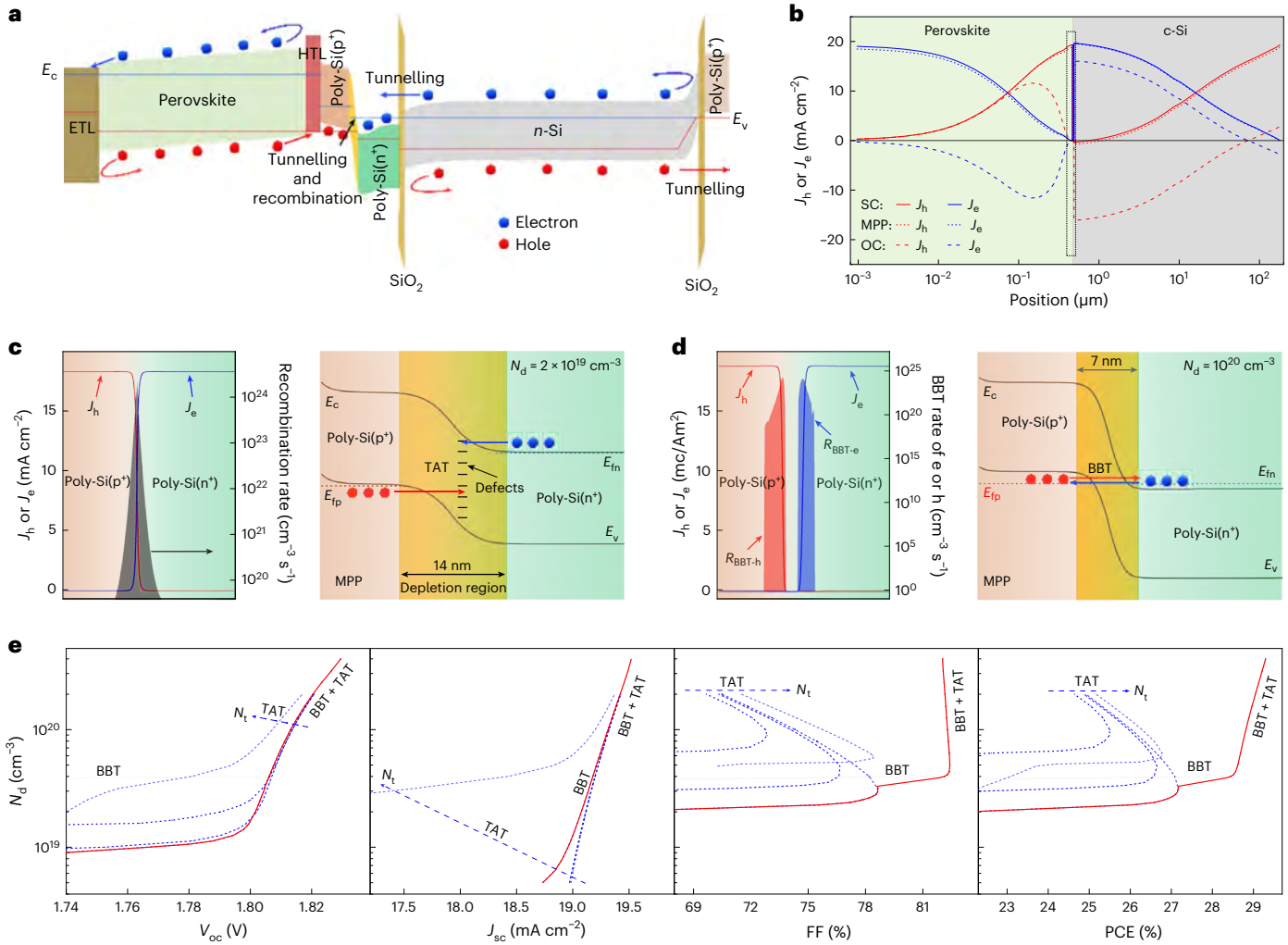

Fig. 5 | Carrier transport mechanisms. a, Energy band diagram of the perovskite/TOPCon TSCs with poly-Si TRL under light equilibrium state. **b**, Profiles of the hole and electron current densities within the device under SC, MPP and OC conditions. **c**,**d**, J_h and J_e distributions, recombination/BBT rates and the corresponding energy diagrams within poly-Si(p^+) and poly-Si(n^+) regions at MPP under doping concentration (N_d) = 2×10^{19} (**c**) and 10^{20} (**d**) cm^{-3}. The defects within the depletion region are depicted by the black dashes in **c**. The background colours of red, yellow and green in **c** and **d** correspond to the B-doping, depletion and P-doping regions, respectively. E_{fn}/E_{fp} and $R_{BBT\text{-}e}/R_{BBT\text{-}h}$ represent electron/hole Fermi level and BBT rate, respectively. **e**, Electrical parameters (that is, V_{oc}, J_{sc}, FF and PCE) as a function of N_d of poly-Si(p^+) and poly-Si(n^+), where the blue, black and red lines represent the results conducted by TAT, BBT and BBT + TAT models, respectively. The blue arrows indicate the increase in defect concentration (N_t) when carriers recombine by TAT. Here type I defect, that is, acceptor-/donor-type defects distributed upon/below the middle bandgap of poly-Si for both poly-Si(p^+) and poly-Si(n^+), was used for simulation. The four blue lines stand for the TAT results with the different N_t, that is, 10^{17}, 10^{18}, 10^{19} and 10^{20} cm^{-3} and BBT (black lines) and BBT + TAT (red lines) results are conducted by $N_t = 10^{19}$ cm^{-3}.

apparent roll off from the peaks. For a high N_d (> 5×10^{19} cm^{-3}), increasing the defect concentrations will result in a decrease in V_{oc} and J_{sc} due to increased recombination losses, but it will also cause an increase in FF and PCE due to the strengthened TAT effect. By balancing the recombination loss and TAT effect, the highest PCE yielding point occurs at N_d = ~3×10^{19} cm^{-3} for $N_t = 10^{19}$ cm^{-3}. Then, we take $N_t = 10^{19}$ cm^{-3} as an example to show the effect of BBT on device performance. The BBT results (black lines), where TAT is absent, hint that BBT does not work if $N_d < 4 \times 10^{19}$ cm^{-3}, which is the critical value of energy band overlap between poly-Si(p^+) and poly-Si(n^+). Once activated, BBT becomes the dominant transport mechanism for the poly-Si(p^+)/poly-Si(n^+) junction, as the response of BBT is essentially the same as that of TAT + BBT (red lines). In the presence of BBT (for both BBT and TAT + BBT cases), the electrical parameters (except for FF) show an increasing trend with the increase of N_d from 10^{19} to 4×10^{20} cm^{-3}, suggesting that higher N_d is conducive to promoting device performance. This conclusion accounts for the experimental observations that TR-free tandems often receive poor device performance[8,19,38,39], especially for FF and PCE, where the correlative functional layers between the top and bottom sub-cells may have mismatched energy-level alignment or recombination mechanisms. Moreover, cases with different types of defect were also checked with consistent conclusions as above (Supplementary Figs. 32–36). Moreover, these simulation results also indicated that when the doping concentration is low, carrier tunnelling is sensitive to defect concentration that is primarily dominated by TAT, resulting in lower FF and efficiency. Conversely, when the doping concentration is high, carrier tunnelling that is basically independent of defect concentration is primarily dominated by BBT, leading to higher FF and efficiency. Therefore, considering that the experimental doping concentration here is ~10^{20} cm^{-3}, the device performance should be almost unaffected by the defect concentration. These findings provide insights into the relationship between doping concentration and device performance, and the simulation results helped us derive the correlation between doping concentration and device characteristics.

Certainly, our conclusions have broad applicability, not only to the poly-Si but also to other material systems.

Conclusion

In this study, we demonstrated the use of a poly-Si TRL as an effective means of constructing perovskite/TOPCon TSCs. By suppressing dopant interdiffusion and compensation, a high doping concentration with a sharp dopant boundary at the poly-Si(p^+)/poly-Si(n^+) interface was obtained, thereby suggesting the form of a high-quality TJ. Furthermore, we found that the SiO_2-based poly-Si(p^+) substrate exhibited superior adsorption abilities for MeO-2PACz compared with that of the IZO counterpart, resulting in an improved charge-carrier transport and extraction, particularly for the top perovskite sub-cells. We also conducted a comprehensive theoretical analysis of the carrier transport/tunnelling mechanisms of perovskite/TOPCon TSCs with this type of poly-Si TRL, which revealed that carrier transport through BBT is critical for achieving high FF and efficiency. As a result of these advantages, perovskite/TOPCon TSC with poly-Si TRL achieved a remarkable efficiency of 29.2%, significantly higher than that of conventional IZO-based TSC (28%). Additionally, the perovskite/TOPCon TSC with poly-Si TRL presents great stability, retaining 85% of its initial PCE after 500 hours under continuous xenon-lamp illumination without filtering ultraviolet in the air (RH = 40–70%, T = 20–35 °C) of MPP tracking. The results presented in this study concerning the RL designs and transport/tunnelling mechanisms of TSCs are expected to stimulate new research hotspots and accelerate the industrialization of perovskite/TOPCon TSCs. Importantly, this research may have significant implications for the future of the PV industry as it represents a step towards the development of a more efficient and cost-effective technology for large-scale energy production.

Methods

Measurements and characteristics

The HR-TEM samples (cross-sectional lamella) were obtained by a standard focused ion beam procedure and ex-situ lift out (Helios-G4-CX), and the TEM characterization was performed using a high-resolution transmission electron microscopy (Talos F200X). EDS was carried out using four in-column Super-X detectors. The cross-sectional SEM images were obtained by SEM equipment (Regulus SU8230, Hitachi). Light J–V curves were measured using a Keithley 2400 source meter under a light intensity of 100 mW cm^{-2} from the Class AAA solar simulator (EnliTech), which has been calibrated with a certified reference solar cell (National Renewable Energy Laboratory). Without any light soaking or electric-poling preconditioning, light J–V curves of tandem devices were measured under a scanning speed of 200 mV s^{-1} in both forward and reverse scan directions with the voltage range from −0.1 to +1.9 V. Here the measurements of the two types of TSC were performed in the same measurement batch, which is known to exhibit higher reproducibility. For stability measurement, the tandem device was simply encapsulated and was tested under MPP condition at the regular air ambient environment (RH = 40–70%, T = 20–35 °C). To assess the stability of the tandem device, a simple encapsulation method was employed. Specifically, the device was positioned between two ordinary glass pieces and securely sealed using epoxy resin. Copper wires were drawn from the encapsulated device to serve as positive and negative electrodes. EQE spectra were measured by the QE measurement system (QE-R, EnliTech.). The light intensity for EQE measurement at different wavelengths has been calibrated with standard single-crystal Si (300–1,100 nm) and Ge (800–1,200 nm) reference solar cells. EQE spectra of perovskite top cell or Si bottom cell were measured independently with a bias voltage of 0.5/1 V by saturating the bottom/top cell with continuous biased light from a white light equipped with a long-pass (>800 nm)/low-pass (<800 nm) filter, respectively. It should be noted that EQE spectra were measured without encapsulation in ambient air. C–V measurement was carried out by an electrochemical workstation under 100 kHz. For TOPCon passivation samples, the passivation parameters including iV_{oc} and τ_{eff} were extracted by the photo-conductance decay technique (WCT-120, Sinton) instrument, where the details were demonstrated in Supplementary Note 1. The profiles of active carrier concentration were obtained by the ECV system (Buchanan, CVP21). The I–V curves used for extracting contact performance were measured using a semiconductor parameter analyser (Keithley 4200-SCS) under the different metal dots with the corresponding diameters of 1.6, 1.8, 2.0 and 2.4 mm. Photoluminescence images were obtained by an EPL system (EPL-P500+, Ai-SHINE). The sample with poly-Si(p^+)/poly-Si(n^+)/SiO_x/n-Si structure was used for SIMS measurement with an etch step of 0.6 nm. The chemical compositions, work function and surface potential were analysed by FTIR (Thermo, Nicolet 6700), XPS/UPS (AXIS ULTRA DLD) and top-view KPFM measurement (Dimension ICON SPM). The quartz substrates were used for steady-state PL, TrPL and fs-TA measurements. Steady-state PL spectra were obtained by a fluorescence spectrometer (FL3-111, HORIBA) with an excitation wavelength of 470 nm. TrPL measurement was performed by an FLS1000 (HORIBA) with an excitation wavelength of 457 nm illuminated from the quartz side. The measurement was conducted at an energy of 9.5 μJ cm^{-2} with a repetition rate of 200 KHz and a laser spot size of ~2 μm. The fs-TA measurement was performed on a Helios pump-probe system (Ultrafast Systems) combined with an amplified femtosecond laser system (TOPAS-800-fs), where the illumination is from the quartz side, and the pump pulse wavelength is 520 nm. The pump pulse was excited by a Ti:sapphire regenerative amplifier (Legend Elite-1K-HE; 800 nm), 35 fs, 7 mJ per pulse, 1 kHz) and seeded with a mode-locked Ti:sapphire laser system (Micra 5) and an Nd:YLF laser (EvolutIon 30) pumped. Focusing the 800 nm beams (split from the regenerative amplifier with a tiny portion, 0.01 mW) onto a sapphire plate produced the white light continuum (WLC) probe pulses (430–770 nm). The pulse-to-pulse fluctuation of the WLC is corrected by a reference beam split from WLC. A motorized optical delay line was used to change the time delays (0–8 ns) between the pump and probe pulses. The instrument response function was determined to be ~100 fs by a routine cross-correlation procedure. A mechanical chopper operated at a frequency of 500 Hz is used to modulate the pump pulses such that the fs-TA spectra with and without the pump pulses can be recorded alternately. The temporal and spectral profiles (chirp-corrected) of the pump-induced differential transmission of the WLC probe light (that is, absorbance change) were visualized by an optical fibre-coupled multichannel spectrometer (with a CMOS sensor) and further processed by the Surface X-plorer software.

TOPCon solar cell preparation

The n-type (100)-oriented polished Czochralski (Cz) silicon wafers with a resistivity of 1–3 Ω cm, and a thickness of 270 μm were used to fabricate the TOPCon solar cells. The commercial solar cells feature thinner silicon wafers, around 150 μm. Whereas the use of a thicker 270 μm silicon wafer in this study may enhance optical absorption, it is essential to note that this variation does not alter the main results and conclusions of this paper. First, the random pyramids were prepared by soaking the wafers in 80 °C KOH solution (0.27 mol l^{-1}) for 10 min. Then, a standard RCA cleaning procedure was implemented to remove the contamination of organic compounds and metal irons on Si surfaces. After that, an ultrathin SiO_x film (~1.7 nm) followed by a phosphorus-doped/boron-doped a-Si:H (~15/30 nm) was deposited on the front/rear side of Si substrates by a plasma-enhanced chemical vapour deposition (PECVD) system (Model-FE-PECVD-L-2)[40], in which SiO_x was prepared by the plasma-assisted nitrous-oxide (N_2O) gas oxidation (PANO) method[41]. The reaction gases used for PECVD deposition include silane (SiH_4), borane (B_2H_6), phosphine (PH_3), hydrogen (H_2) and methane (CH_4). In addition, CH_4 was also included as the reaction gas when preparing N-doped poly-Si films with the purpose of preventing film blistering[42,43]. A high-temperature furnace annealing

at 900–960 °C for 30 min was performed to crystallize a-Si:H films into poly-Si. For the TJ-TOPCon SCs, a two-step annealing method was utilized to prevent interdiffusion in the poly-Si(n^+)/poly-Si(p^+) TJ. In the first step, the poly-Si(n^+) layer was prepared through a high-temperature annealing process ranging from 900 °C to 960 °C. This initial annealing step helped establish a stable and well-defined poly-Si(n^+) layer. Subsequently, the a-Si(p^+) layers were overlaid on top of the poly-Si(n^+) layer. To prevent interdiffusion, only a rapid annealing step at 700 °C was conducted using a rapid thermal annealing (RTA) equipment (RTP-300) to crystallize a-Si(p^+) into poly-Si(p^+)[44]. After that, samples were covered by an ~15 nm alumina (Al_2O_3) film prepared by atomic layer deposition followed by the annealing at 450 °C for 30 min in the N_2 atmosphere for hydrogen injection. Then, a hydrofluoric acid (HF) dip for 30 s was carried out to remove the Al_2O_3 film, and an 80 nm-thick ITO film (90% In_2O_3/10% SnO_2, 99.9%, Zhong Nuo Advanced Material Technology) was deposited on the front side of the samples by physical vapour sputtering (Sky Technology Development) followed by a 10 min hot plate annealing at 250 °C to recover the sputtering damage. Finally, a stack of 20 nm Cr/20 nm Pd/300 nm Ag metal of fish-bone fingers was deposited by an electron beam deposition equipment with a shadow mask on the TCO layer, and the 1 nm Cr/250 nm Ag full area films were realized by thermal evaporation (FE Thin Film) as the rear-sided metal electrode.

Tandem solar cell preparation

For the tandem devices, the front and rear sides of Si wafers were textured by reconstructed black silicon structures[3] and random micro-pyramids, respectively, to improve the optical response, in which the purpose of using reconstructed black silicon is to be compatible with the preparation of perovskite film. The preparation processes of TOPCon structures for tandems are the same as that of TOPCon SCs. For the RL tandems, the interlayer, that is, an ~15 nm transparent IZO film (90% In_2O_3/10% ZnO, 99.9%, Zhong Nuo Advanced Material Technology) was deposited upon poly-Si(n^+) by a PVD system and followed by a 250 °C hot plate annealing for 10 min. Then, for both IZO RL and poly-Si TRL samples, the full area Cr (1 nm)/Ag (250 nm) films were deposited by thermal evaporation (FE Thin Film) as the rear-sided metal electrode. After that, samples were treated in a UV–ozone cleaner for 15 min to remove the surface contamination. After the samples were transferred into a dry nitrogen-filled glovebox (<10 ppm O_2), MeO-2PACz solution (1 mg ml^{-1} in anhydrous ethanol) was spin coated on the top of the IZO or poly-Si(p^+) layer followed by a hot plate at 100 °C for 10 min to dry the samples. Following that, the perovskite precursor solution was spin coated upon MeO-2PACz for 35 s with a speed of 3,500 r.p.m. During the spin process, chlorobenzene was dropped by the one-step anti-solvent recipe. A 100 °C hot plate for 15 min was then performed to form the CsFAMA-mixed perovskite film (that is, $Cs_{0.05}(FA_{0.83}MA_{0.17})_{0.95}Pb(I_{0.83}Br_{0.17})_3$). Next, a 20 nm C60 together with a buffer layer (BCP:Ag of 10:1 nm) was deposited by thermal evaporation. A 100 nm-thick IZO was sputtered by a PVD system with a radiofrequency power of 80 W. The Ag films (250 nm) were then evaporated on top of samples by the thermal evaporation system with a shadow mask to define the aperture area of the device (0.1 cm^2). Finally, a 120 nm LiF_x antireflection film was evaporated on the top side of the devices at a rate of 1 Å s^{-1}.

DFT and finite element simulation

For DFT simulation, the Vienna Ab-initio Simulation Package code was used[45,46]. The pseudopotential of the projector augmented wave is used to describe the core–valence electron interaction. The Perdew–Burke–Ernzerhof functional within the generalized gradient approximation is carried out to handle the exchange functional. All calculated energy cut-off settings were set to 450 eV. The force convergence of structural relaxation is set to less than 0.02 eV $Å^{-1}$ and a Γ-centred 2 × 2 × 1 k-point mesh is used to sample the Brillouin zone. The lattice parameters for the bulk In_2O_3, SiO_2, and Si were listed in the table (Supplementary Table 6). The bulk In_2O_3, SiO_2, Si are cut along the (0, 0, 1) planes and expanded as 2 × 2 × 1 supercell (In_2O_3 (001), SiO_2 (001), Si (001)). 20 Å vacuum layers were added to the supercells at the same time to eliminate the interactions between periodic images. A part of In atoms in In_2O_3 (001) was replaced by Zn atoms to construct 10% Zn doped In_2O_3 (001), and a part of Si atoms in Si (001) were replaced by B atoms to construct 3% B doped Si (001). The binding energy of the three structures, that is, 10% Zn doped In_2O_3 (001), SiO_2 (001), 3% B doped Si (001), with a MeO-2PACz molecule was calculated according to the formula: $E_b = E$(slab-MeO-2PACz) – E(slab) – E(MeO-2PACz). Here slab represents three types of structures, that is, 10% Zn doped In_2O_3 (001), SiO_2 (001), 3% B doped Si (001), E(slab-MeO-2PACz) is the total energy of slab-MeO, where E(slab) is the total energy of slab and E(MeO-2PACz) is the total energy of MeO-2PACz molecule. Charge difference and bader charge analysis were calculated to investigate the charge transfer between the substrates and MeO-2PACz molecule. To calculate the strength of bonds among the atoms of three types of structures and MeO-2PACz molecule, the COHP and ICOHP for the related bonds were simulated. The LOBSTER and wxDRAGON software were used for COHP and ICOHP calculations[26–28]. For the finite element simulation, Silvaco TCAD was employed[47], and the calculated details were displayed in Supplementary Note 2 and Supplementary Table 7. First, the optical simulation was carried out by solving Maxwell's equations to obtain the frequency-dependent and spatial-dependent electromagnetic distributions[48]. In that case, the optical properties including optical absorption efficiency and optical generation rate can be thus obtained. On the basis of the optical results (that is, spatial-dependent photogeneration rate), the electrical simulation was then carried out by addressing Poisson's equation and carrier transport equations. By solving these equations, carrier generation, transport, recombination and extraction behaviour can be clarified, and parameters including spatial distribution of hole and electron concentration and potential can be obtained so that the related device performance concerning electrical parameters (that is, V_{oc}, J_{sc}, FF and PCE) can be extracted.

Reporting summary

Further information on research design is available in the Nature Portfolio Reporting Summary linked to this article.

Data availability

All data generated or analysed during this study are included in the published article and its Supplementary Information. Any additional information is available from corresponding authors upon request. Source data are provided with this paper.

References

1. Richter, A., Hermle, M. & Glunz, S. W. Reassessment of the limiting efficiency for crystalline silicon solar cells. *IEEE J. Photovoltaics* **3**, 1184–1191 (2013).
2. Schafer, S. & Brendel, R. Accurate calculation of the absorptance enhances efficiency limit of crystalline silicon solar cells with Lambertian light trapping. *IEEE J. Photovoltaics* **8**, 1156–1158 (2018).
3. Ying, Z. et al. Monolithic perovskite/black-silicon tandems based on tunnel oxide passivated contacts. *Joule* **6**, 2644–2661 (2022).
4. Tockhorn, P. et al. Nano-optical designs for high-efficiency monolithic perovskite-silicon tandem solar cells. *Nat. Nanotechnol.* **17**, 1214–1221 (2022).
5. Sveinbjörnsson, K. et al. Monolithic perovskite/silicon tandem solar cell with 28.7% efficiency using industrial silicon bottom cells. *ACS Energy Lett.* **7**, 2654–2656 (2022).
6. Mailoa, J. P. et al. A 2-terminal perovskite/silicon multijunction solar cell enabled by a silicon tunnel junction. *Appl. Phys. Lett.* **106**, 121105 (2015).
7. Best research-cell efficiencies. *NREL* https://www.nrel.gov/pv/cell-efficiency.html (2023).

8. Shen, H. et al. In situ recombination junction between *p*-Si and TiO_2 enables high-efficiency monolithic perovskite/Si tandem cells. *Sci. Adv.* **4**, eaau9711 (2018).
9. Bush, K. A. et al. 23.6%-efficient monolithic perovskite/silicon tandem solar cells with improved stability. *Nat. Energy* **2**, 17009 (2017).
10. Zheng, J. et al. Large area efficient interface layer free monolithic perovskite/homo-junction-silicon tandem solar cell with over 20% efficiency. *Energy Environ. Sci.* **11**, 2432–2443 (2018).
11. Sahli, F. et al. Fully textured monolithic perovskite/silicon tandem solar cells with 25.2% power conversion efficiency. *Nat. Mater.* **17**, 820–826 (2018).
12. Hou, Y. et al. Efficient tandem solar cells with solution-processed perovskite on textured crystalline silicon. *Science* **367**, 1135–1140 (2020).
13. Kim, D. et al. Efficient, stable silicon tandem cells enabled by anion engineered wide-bandgap perovskite. *Science* **368**, 155–160 (2020).
14. Xu, J. et al. Triple-halide wide-band gap perovskites with suppressed phase segregation for efficient tandems. *Science* **367**, 1097–1104 (2020).
15. Aydin, E. et al. Ligand-bridged charge extraction and enhanced quantum efficiency enable efficient n–i–p perovskite/silicon tandem solar cells. *Energy Environ. Sci.* **14**, 4377–4390 (2021).
16. Al-Ashouri, A. et al. Monolithic perovskitesilicon tandem solar cell with 29% efficiency by enhanced hole extraction. *Science* **370**, 1300–1309 (2020).
17. De Bastiani, M. et al. Recombination junctions for efficient monolithic perovskite-based tandem solar cells: physical principles, properties, processing and prospects. *Mater. Horiz.* **7**, 2791–2809 (2020).
18. Palmstrom, A. F. et al. Enabling flexible all-perovskite tandem solar cells. *Joule* **3**, 2193–2204 (2019).
19. Zheng, J. et al. Large-area 23%-efficient monolithic perovskite/homojunction-silicon tandem solar cell with enhanced UV stability using down-shifting material. *ACS Energy Lett.* **4**, 2623–2631 (2019).
20. Sahli, F. et al. Improved optics in monolithic perovskite/silicon tandem solar cells with a nanocrystalline silicon recombination junction. *Adv. Energy Mater.* **8**, 1701609 (2017).
21. Aydin, E. et al. Interplay between temperature and bandgap energies on the outdoor performance of perovskite/silicon tandem solar cells. *Nat. Energy* **5**, 851–859 (2020).
22. Peibst, R. et al. From PERC to tandem: polo- and p^+/n^+ poly-Si tunneling junction as interface between bottom and top cell. *IEEE J. Photovoltaics* **9**, 49–54 (2019).
23. Luderer, C. et al. Controlling diffusion in poly-Si tunneling junctions for monolithic perovskite/silicon tandem solar cells. *IEEE J. Photovoltaics* **11**, 1395–1402 (2021).
24. *Trends in PV Applications* (IEA, 2023); https://iea-pvps.org/publications/
25. Boccard, M. & Ballif, C. Influence of the subcell properties on the fill factor of two-terminal perovskite–silicon tandem solar cells. *ACS Energy Lett.* **5**, 1077–1082 (2020).
26. Nelson, R. et al. LOBSTER: local orbital projections, atomic charges, and chemical bonding analysis from projector-augmented-wave-based DFT. *J. Comput. Chem.* **41**, 1931–1940 (2020).
27. Maintz, S., Deringer, V. L., Tchougreeff, A. L. & Dronskowski, R. LOBSTER: a tool to extract chemical bonding from plane-wave based DFT. *J. Comput. Chem.* **37**, 1030–1035 (2016).
28. Richard Dronskowski, P. E. B. Crystal orbital Hamilton populations (COHP): energy-resolved visualization of chemical bonding in solids based on density-functional calculations. *J. Phys. Chem.* **97**, 8617–8624 (1993).
29. Botta, A. et al. Synthesis, characterization, and use as emissive layer of white organic light emitting diodes of the highly isotactic poly(N-pentenyl-carbazole). *Polym. Compos.* **36**, 1110–1117 (2015).
30. Sun, J. et al. NiO_x-seeded self-assembled monolayers as highly hole-selective passivating contacts for efficient inverted perovskite solar cells. *Sol. RRL* **5**, 2100663 (2021).
31. Pellerite, M. J., Dunbar, T. D., Boardman, L. D. & Wood, E. J. Effects of fluorination on self-assembled monolayer formation from alkanephosphonic acids on aluminum: kinetics and structure. *J. Phys. Chem. B* **107**, 11726–11736 (2003).
32. Raman, A., Dubey, M., Gouzman, I. & Gawalt, E. S. Formation of self-assembled monolayers of alkylphosphonic acid on the native oxide surface of SS316L. *Langmuir* **22**, 6469–6472 (2006).
33. Al-Ashouri, A. et al. Conformal monolayer contacts with lossless interfaces for perovskite single junction and monolithic tandem solar cells. *Energy Environ. Sci.* **12**, 3356–3369 (2019).
34. Liao, J.-F. et al. Enhanced efficacy of defect passivation and charge extraction for efficient perovskite photovoltaics with a small open circuit voltage loss. *J. Mater. Chem. A* **7**, 9025–9033 (2019).
35. Zhang, J. et al. $CsPbBr_3$ nanocrystal induced bilateral interface modification for efficient planar perovskite solar cells. *Adv. Sci.* **8**, e2102648 (2021).
36. Liu, X. et al. Full defects passivation enables 21% efficiency perovskite solar cells operating in air. *Adv. Energy Mater.* **10**, 2001958 (2020).
37. Messmer, C., Bivour, M., Schon, J., Glunz, S. W. & Hermle, M. Numerical simulation of silicon heterojunction solar cells featuring metal oxides as carrier-selective contacts. *IEEE J. Photovoltaics* **8**, 456–464 (2018).
38. Hyun, J. et al. Efficient n–i–p monolithic perovskite/silicon tandem solar cells with tin oxide via a chemical bath deposition method. *Energies* **14**, 7614 (2021).
39. Li, W. et al. High-performance solar flow battery powered by a perovskite/silicon tandem solar cell. *Nat. Mater.* **19**, 1326–1331 (2020).
40. Wei, H. et al. Unraveling the passivation mechanisms of c-Si/SiO_x/poly-Si contacts. *Sol. Energy Mater. Sol. Cells* **250**, 112047 (2023).
41. Huang, Y. et al. Ultrathin silicon oxide prepared by in-line plasma-assisted N_2O oxidation (PANO) and the application for *n*-type polysilicon passivated contact. *Sol. Energy Mater. Sol. Cells* **208**, 110389 (2020).
42. Zheng, J. et al. Blistering-free polycrystalline silicon carbide films for double-sided passivating contact solar cells. *Sol. Energy Mater. Sol. Cells* **238**, 111586 (2022).
43. Lin, Y. et al. Dual-functional carbon-doped polysilicon films for passivating contact solar cells: regulating physical contacts while promoting photoelectrical properties. *Energy Environ. Sci.* **14**, 6406–6418 (2021).
44. Shou, C. et al. Optimization of tunnel-junction for perovskite/tunnel oxide passivated contact (TOPCon) tandem solar cells. *Phys. Status Solidi A* **218**, 2100562 (2021).
45. Kresse, G. & Furthmiiller, J. Efficiency of ab-initio total energy calculations for metals and semiconductors using a plane-wave basis set. *Comp. Mater. Sci.* **6**, 15–50 (1996).
46. Yi, W., Tang, G., Chen, X., Yang, B. & Liu, X. qvasp: a flexible toolkit for VASP users in materials simulations. *Comput. Phys. Commun.* **257**, 107535 (2020).
47. TCAD (Silvaco, 2023); https://silvaco.com/tcad/
48. Yang, Z. et al. Device physics of back-contact perovskite solar cells. *Energy Environ. Sci.* **13**, 1753–1765 (2020).

Acknowledgements

X.L. acknowledges financial support from the National Key Research and Development of China (grant number 2022YFB4200901). J.Y. acknowledges financial support from the Zhejiang Energy Group (project number znkj-2018-118) and Ningbo 'Innovation 2025' Major Project (2020Z098, 2022Z114). Z. Yang acknowledges financial support from the National Natural Science Foundation

of China (62004199). Y.Z. acknowledges financial support from the Key Research and Development Program of Zhejiang Province (2021C01006) and Youth Innovation Promotion Association (2018333).

Author contributions

J.Z. fabricated the TOPCon bottom cells and interlayers, did most of the measurements and wrote the first version of the paper. Z. Ying fabricated the perovskite top cells and tested the tandem devices. J.Z. and Z. Yang conceived the idea, designed the experiments and wrote the paper. Z.L. and Z. Yang contributed to the DFT and finite element simulation. H.W. contributed to the fabrication of the TOPCon bottom cells and relative tests. L.C. performed the TEM measurement. X.Y. contributed to the design of the structure of tandem cells. Y.Z. provided the resources for the experiments. X.L. supervised the project and revised the paper. J.Y. supervised the project and revised the paper.

Competing interests

The authors declare no competing interests.

Additional information

Supplementary information The online version contains supplementary material available at https://doi.org/10.1038/s41560-023-01382-w.

Correspondence and requests for materials should be addressed to Zhenhai Yang, Xi Yang, Xiaofeng Li or Jichun Ye.

Peer review information *Nature Energy* thanks Jan Christoph Goldschmidt, Robby Peibst and Arthur Weeber for their contribution to the peer review of this work.

nature research

Corresponding author(s): Zhenhai yang, Xi Yang, Xiaofeng Li, Jichun Ye

Solar Cells Reporting Summary

Nature Research wishes to improve the reproducibility of the work that we publish. This form is intended for publication with all accepted papers reporting the characterization of photovoltaic devices and provides structure for consistency and transparency in reporting. Some list items might not apply to an individual manuscript, but all fields must be completed for clarity.

For further information on Nature Research policies, including our data availability policy, see Authors & Referees.

Experimental design

Please check: are the following details reported in the manuscript?

1. Dimensions

Area of the tested solar cells	☒ Yes ☐ No	0.1cm2 aperture area was used. All details are in "Tandem solar cell preparation" in "Method" section in the main text.
Method used to determine the device area	☒ Yes ☐ No	Using masks to define device area, see "Tandem solar cell preparation" in "Method" section in manuscript

2. Current-voltage characterization

Current density-voltage (J-V) plots in both forward and backward direction	☒ Yes ☐ No	J-V curves in Figure 1 in the main text.
Voltage scan conditions *For instance: scan direction, speed, dwell times*	☒ Yes ☐ No	The voltage scan were done both Jsc to Voc and Voc to Jsc under the scan speed of 200 mV/s and the dwell time was not applied. All details are in "Measurements and characteristics" in "Method" section in the main text.
Test environment *For instance: characterization temperature, in air or in glove box*	☒ Yes ☐ No	All details about the measurement conditions are in "Measurements and characteristics" in "Method" section in the main text.
Protocol for preconditioning of the device before its characterization	☒ Yes ☐ No	No light soaking or electric-poling preconditioning. Details are in "Measurements and characteristics" in "Method" section in the main text.
Stability of the J-V characteristic *Verified with time evolution of the maximum power point or with the photocurrent at maximum power point; see ref. 7 for details.*	☐ Yes ☒ No	not necessary.

3. Hysteresis or any other unusual behaviour

Description of the unusual behaviour observed during the characterization	☐ Yes ☒ No	not relevant.
Related experimental data	☐ Yes ☒ No	not relevant.

4. Efficiency

External quantum efficiency (EQE) or incident photons to current efficiency (IPCE)	☒ Yes ☐ No	Figure 1e in the main text.
A comparison between the integrated response under the standard reference spectrum and the response measure under the simulator	☐ Yes ☒ No	not relevant.
For tandem solar cells, the bias illumination and bias voltage used for each subcell	☒ Yes ☐ No	in "Measurements and characteristics" in "Method" section in the main text.

5. Calibration

Light source and reference cell or sensor used for the characterization	☒ Yes ☐ No	For in house measurements, Class AAA solar simulator was calibrated by using NREL certified c-Si cell.
Confirmation that the reference cell was calibrated and certified	☒ Yes ☐ No	The reference cell was certified by NREL.

Calculation of spectral mismatch between the reference cell and the devices under test	☐ Yes ☒ No	not relevant.

6. Mask/aperture

Size of the mask/aperture used during testing	☒ Yes ☐ No	In the main text and the certified report in the Supplementary Figure 8.
Variation of the measured short-circuit current density with the mask/aperture area	☐ Yes ☒ No	The results always with aperture, the edge effects are minimized.

7. Performance certification

Identity of the independent certification laboratory that confirmed the photovoltaic performance	☒ Yes ☐ No	Shanghai institute of microsystem and information technology.
A copy of any certificate(s) *Provide in Supplementary Information*	☒ Yes ☐ No	Supplementary Figure 8.

8. Statistics

Number of solar cells tested	☒ Yes ☐ No	Figure 1d and corresponding figure captions in the main text.
Statistical analysis of the device performance	☒ Yes ☐ No	Figure 1d and corresponding figure captions in the main text.

9. Long-term stability analysis

Type of analysis, bias conditions and environmental conditions *For instance: illumination type, temperature, atmosphere humidity, encapsulation method, preconditioning temperature*	☒ Yes ☐ No	Figure 1g and the details in "Measurements and characteristics" in "Method" section in the main text.

nature energy

Article

https://doi.org/10.1038/s41560-023-01382-w

Polycrystalline silicon tunnelling recombination layers for high-efficiency perovskite/tunnel oxide passivating contact tandem solar cells

In the format provided by the authors and unedited

Table of contents

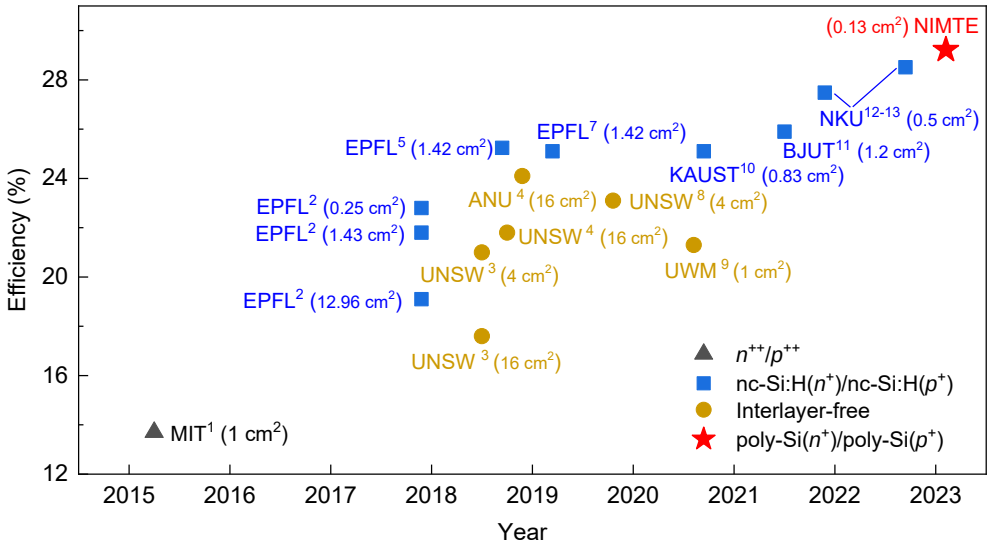

Supplementary Figure 1 | Efficiency statistics of various TSCs. A summary of perovskite/c-Si tandem solar cells with interlayer-free design or various TRLs[1-13].

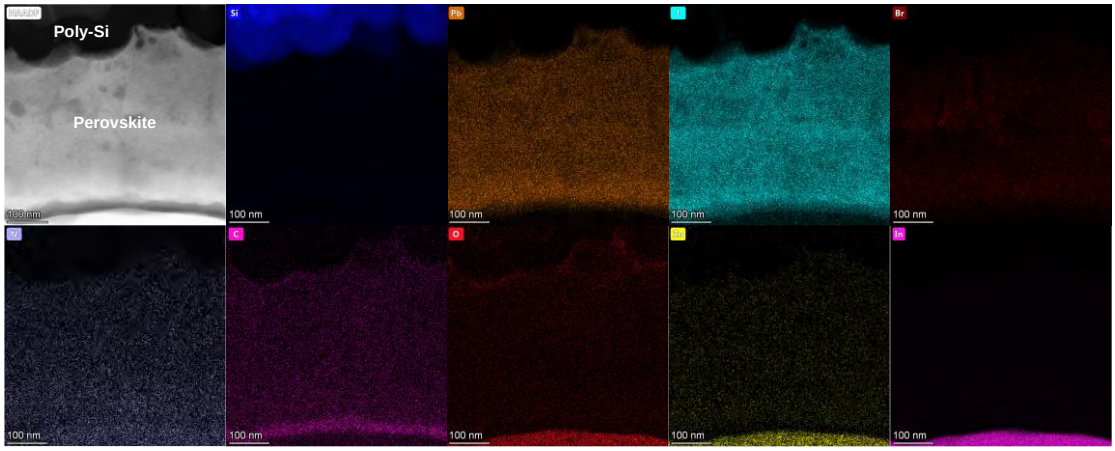

Supplementary Figure 2 | TEM measurement of b-Si sample. EDS mappings (including Si, Pb, I, Br, N, C, O, Zn, and In elements) of b-Si sample.

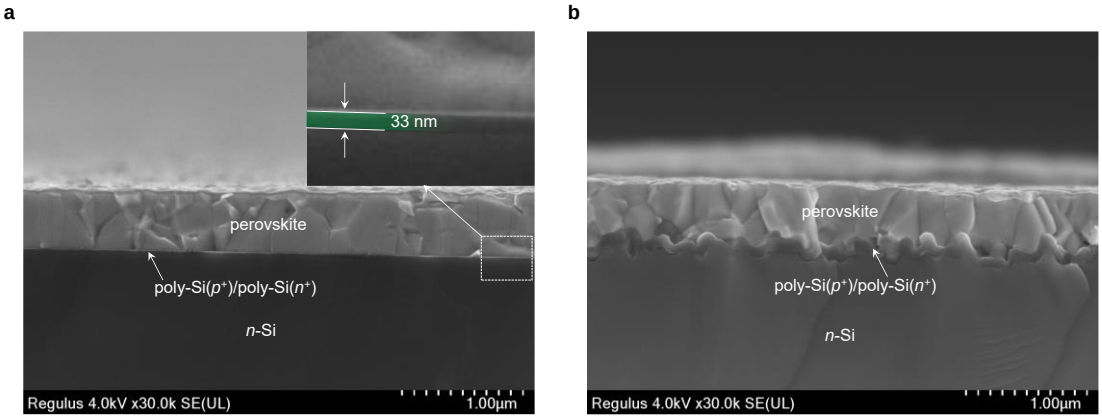

Supplementary Figure 3 | SEM measurements of flat and b-Si samples. SEM images of samples with a structure of perovskite/poly-Si(p^+)/poly-Si(n^+)/SiO_x/n-Si based on (**a**) a flat and (**b**) a b-Si substrate.

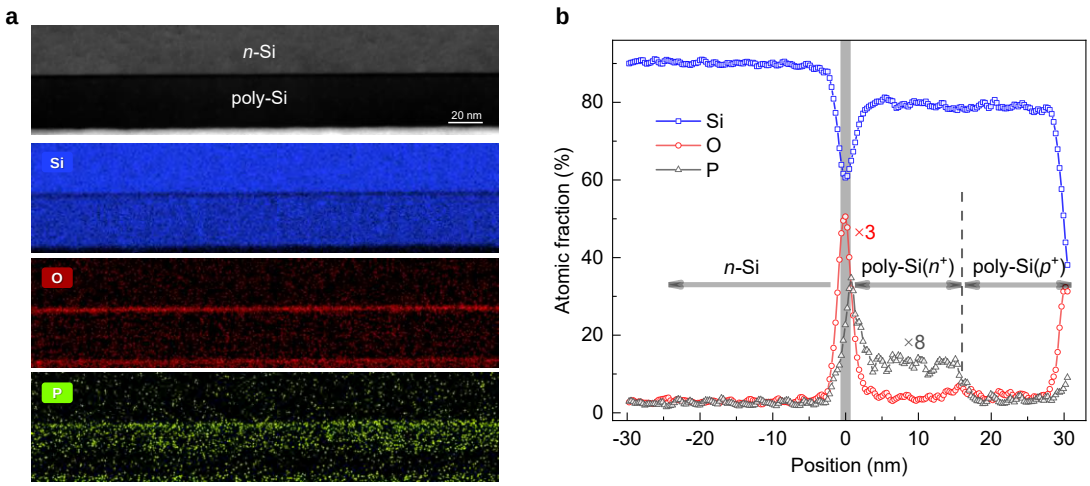

Supplementary Figure 4 | STEM image and corresponding atom profiles. (**a**) STEM image of *n*-Si/SiO_x/poly-Si structure, and EDS mappings of Si, O, and P elements, and (**b**) the corresponding atomic fraction profiles of Si, O, and P elements.

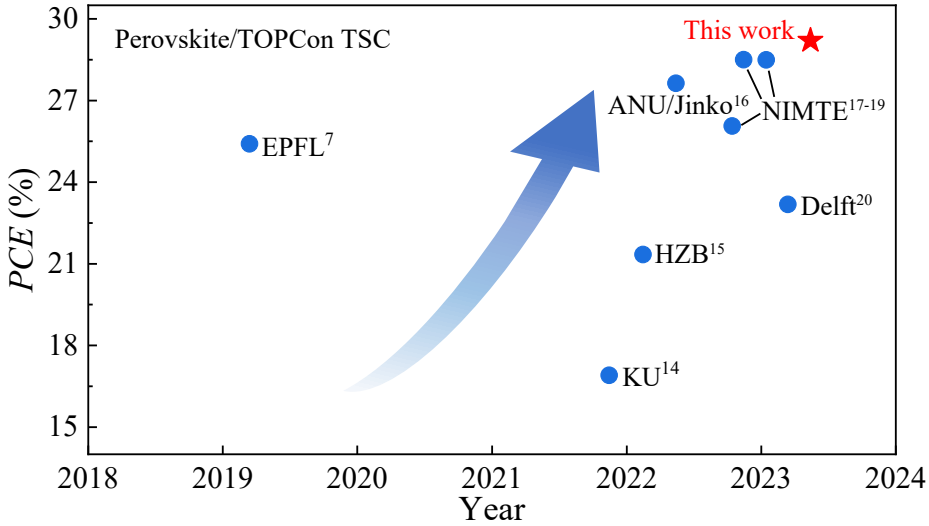

Supplementary Figure 5 | Efficiency statistics of various TSCs. A summary of perovskite/TOPCon tandem solar cells[7,14-20].

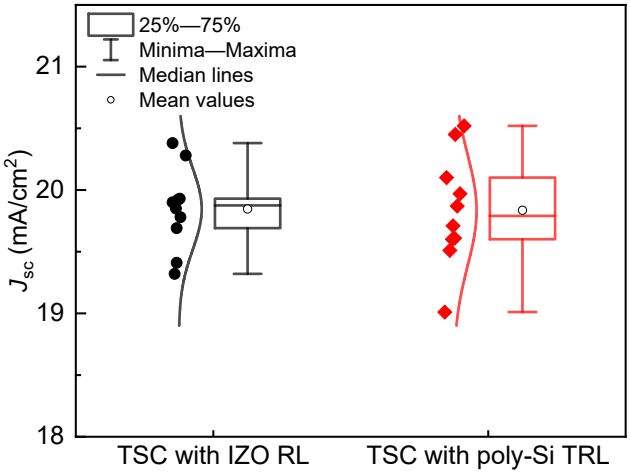

Supplementary Figure 6 | J_{sc} distributions of different samples. Statistical distribution along with the fits (normal distribution of data points) of the J_{sc} values of perovskite/TOPCon TSCs with IZO RL and poly-Si TRL. The lines, arranged from top to bottom, represent the maximum, upper quartile (upper edge of the box), median, lower quartile (lower edge of the box), and minimum values within the dataset. Each experimental condition comprised ten individual samples.

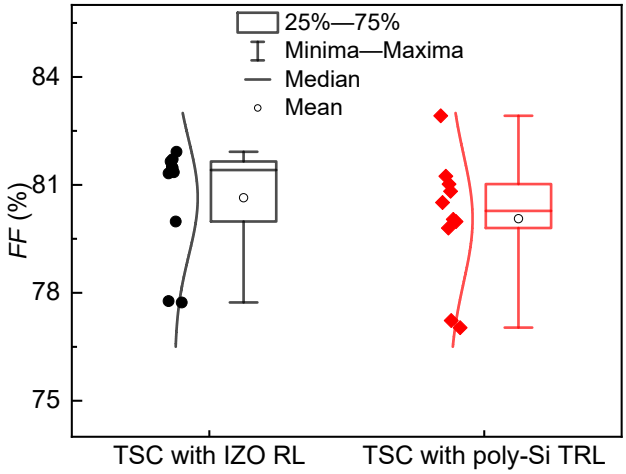

Supplementary Figure 7 | *FF* distributions of different samples. Statistical distribution along with the fits (normal distribution of data points) of the *FF* values of perovskite/TOPCon TSCs with IZO RL and poly-Si TRL. The lines, arranged from top to bottom, represent the maximum, upper quartile (upper edge of the box), median, lower quartile (lower edge of the box), and minimum values within the dataset. Each experimental condition comprised ten individual samples.

Test and Calibration Center of New Energy Device and Module,
Shanghai Institute of Microsystem and Information Technology,
Chinese Academy of Sciences (SIMIT)

Measurement Report

Report No. 22TR111803

Client Name	Ningbo Institute of Materials Technology and Engineering (NIMTE), Chinese Academy of Sciences (CAS)
Client Address	1219 Zhongguan West Road, Ningbo, China (315201)
Sample	Perovskite/Si Tandem Solar Cell
Manufacturer	Ningbo Institute of Materials Technology and Engineering (NIMTE), Jichun Ye Group
Measurement Date	18th November, 2022

Performed by:	Qiang Shi Qiang Shi	**Date:** 18/11/2022
Reviewed by:	Wenjie Zhao Wenjie Zhao	**Date:** 18/11/2022
Approved by:	Zhengxin Liu Zhengxin Liu	**Date:** NOV. 18, 2022

Address: No.235 Chengbei Road, Jiading, Shanghai
Post Code:201800
E-mail: solarcell@mail.sim.ac.cn
Tel: +86-021-69976921

Sample Information

Sample Type	Perovskite/Si Tandem Solar Cell
Serial No.	2-4#
Lab Internal No.	22111801-3#
Measurement Item	I-V characteristic
Measurement Environment	21.9±2.0°C, 35.9±5.0%R.H

Measurement of I-V characteristic

Reference cell	AK-200(Serial No.:2000041)
Reference cell Type	mono-Si, WPVS, calibrated by National Institute of Metrology, China (Certificate No. GXgf2022-01035)
Calibration Value/Date of Calibration for Reference cell	128.1mA/ Apr. 2022
Measurement Conditions	Standard Test Condition (STC): Spectral Distribution: AM1.5 according to IEC 60904-3 Ed.3, Irradiance: 1000±50W/m^2, Temperature: 25±2°C
Measurement Equipment/ Date of Calibration	AAA Steady State Solar Simulator (YSS-T155-2M) / July.2022 IV test system (ADCMT 6246) / June. 2022 SR Measurement system (CEP-25ML-CAS) / April.2022 Measuring Microscope (MF-B2017C) / July.2022
Measurement Method	I-V Measurement: Logarithmic sweep in both directions (Voc to Isc and Isc to Voc) during one flash based on IEC 60904-1:2006; Spectral Mismatch factor was calculated according to IEC 60904-7 and I-V correction according to IEC 60891; MPP-Tracking: Tracking for 300 seconds by P&O method, the reported Pmax represents the average value of the last 60 seconds

====Measurement Results ====

	Forward Scan (Isc to Voc)	Reverse Scan (Voc to Isc)	MPP-Tracking
Active Area		0.1321 cm^2	
Isc	2.530 mA	2.531 mA	/
Voc	1.835 V	1.839 V	/
Pmax	3.775 mW	3.799 mW	3.763 mW
Ipm	2.381 mA	2.387 mA	2.371 mA
Vpm	1.586 V	1.591 V	1.588 V
FF	81.33 %	81.62 %	/
Eff	28.58 %	28.76 %	28.49 %

- Spectral Mismatch Factor: SMM_{top}=1.0007; SMM_{bot}=1.0039
- Active Area was measured by a measuring microscope.
- No temperature control during MPP-Tracking.
- Test results listed in this measurement report refer exclusively to the mentioned measured sample. The results apply only at the time of the test, and do not imply future performance.

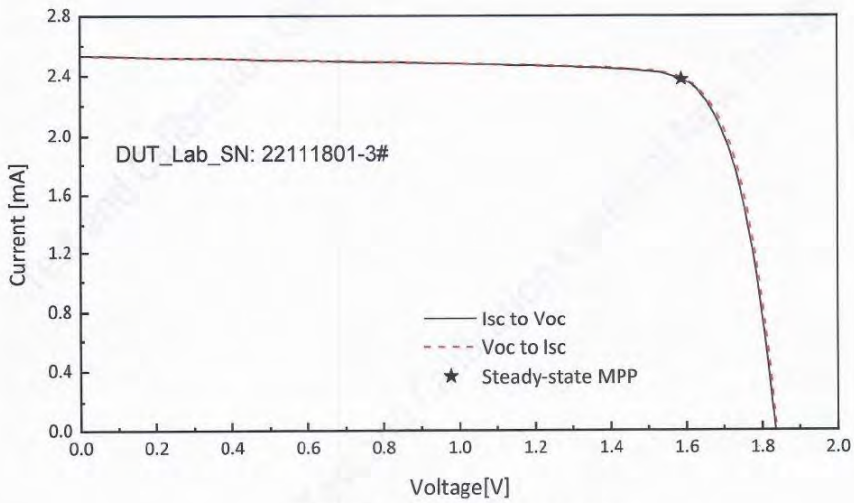

Fig.1 I-V curves of the measured sample

Report No. 22TR111803

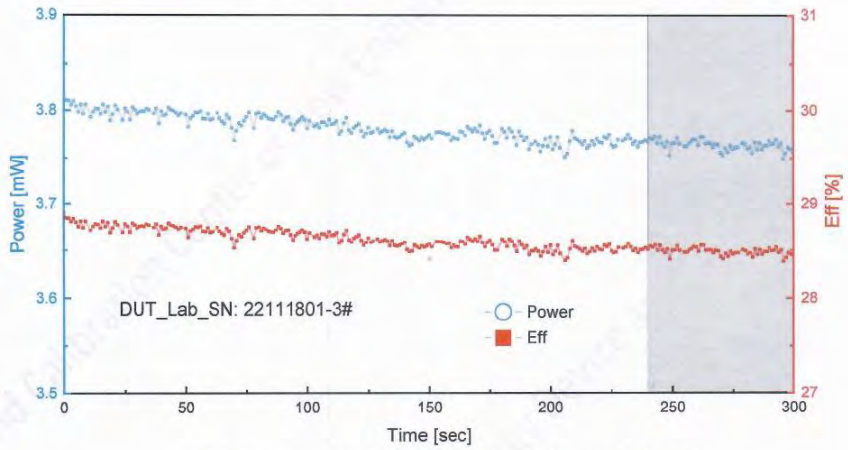

Fig.2 Steady-state maximum power output of the measured sample

====Additional Information ====

Measurement Uncertainty:

Area: 1.1%(k=2); Isc: 1.9%(k=2); Voc: 1.0%(k=2); Pmax: 2.6%(k=2); Eff: 2.8%(k=2)

The uncertainty stated is the expanded uncertainty resulting from multiplying the standard uncertainty by the coverage factor k = 2. The value of the measurand lies with a probability of 95% within the assigned interval.

-------End of Report-------

4 / 4

Supplementary Figure 8 | Certified reports of TSC. Certified reports for the perovskite/TOPCon TSC with poly-Si TRL (0.1321 cm^2).

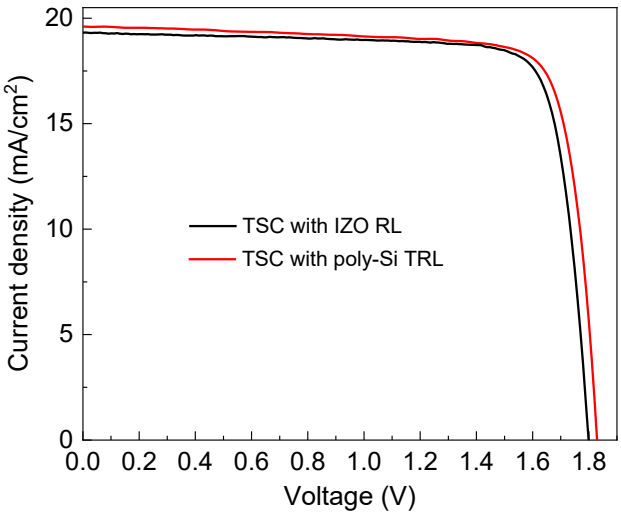

Supplementary Figure 9 | *I-V* curves of the stability samples . Initial *I-V* curves of the two related TSCs for stability tests.

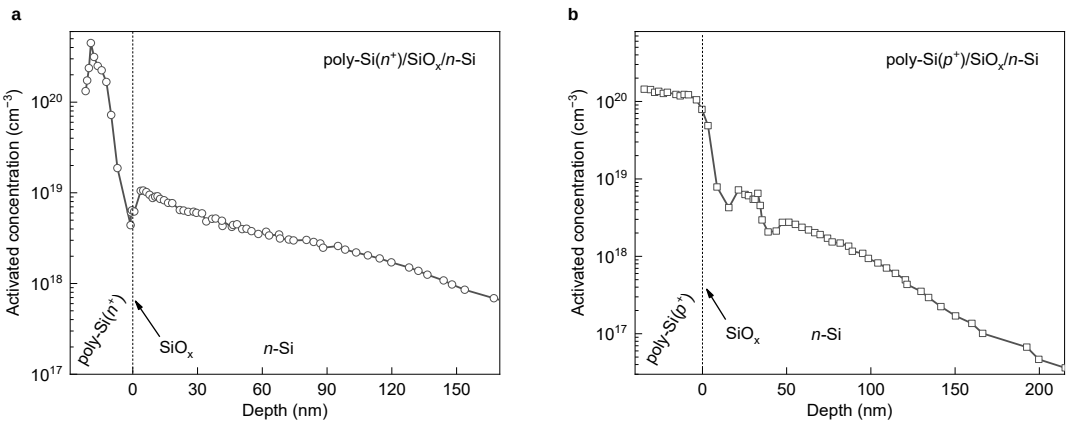

Supplementary Figure 10 | ECV measurements for P and B concentration profiles. Activated P and B concentration profiles for (**a**) poly-Si(n^+)/SiO_x/n-Si and (**b**) poly-Si(p^+)/SiO_x/n-Si samples measured by ECV.

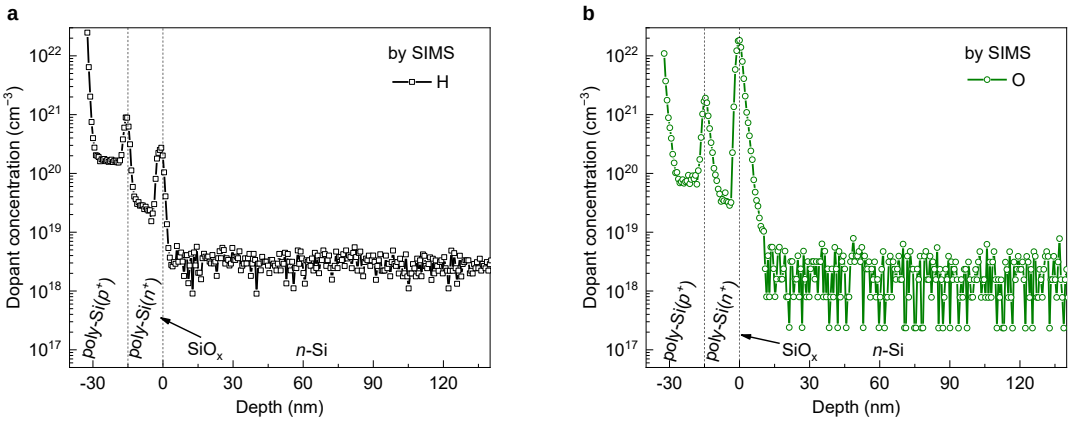

Supplementary Figure 11 | SIMS measurments for H and O concentration. Depth-dependent (**a**) H and (**b**) O concentration profiles for poly-Si(p^+)/poly-Si(n^+)/SiO$_x$/n-Si sample measured by SIMS.

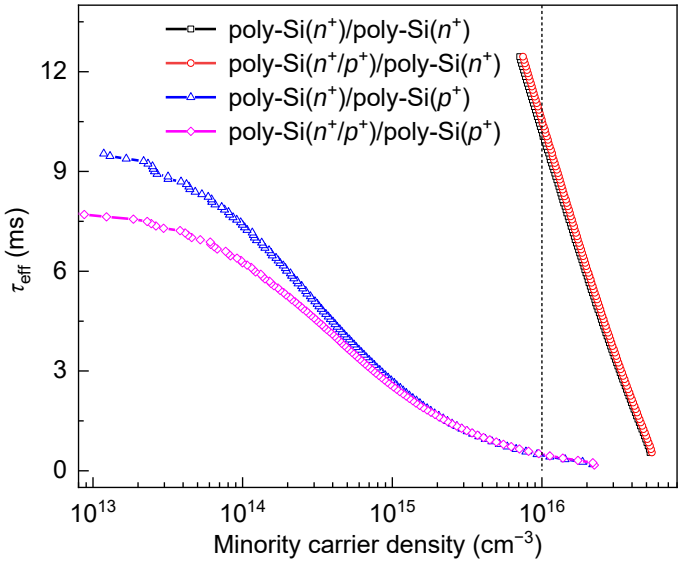

Supplementary Figure 12 | Effective minority carrier lifetime curves of the related samples. Minority carrier density-dependent effective minority carrier lifetime (τ_{eff}) spectra of samples with the different structures, *i.e.*, poly-Si(n^+)/SiO_x/*n*-Si/SiO_x/poly-Si(n^+), poly-Si(p^+)/poly-Si(n^+)/SiO_x/*n*-Si/SiO_x/poly-Si(n^+), poly-Si(n^+)/SiO_x/*n*-Si/SiO_x/poly-Si(p^+), and poly-Si(p^+)/poly-Si(n^+)/SiO_x/*n*-Si/SiO_x/poly-Si(p^+).

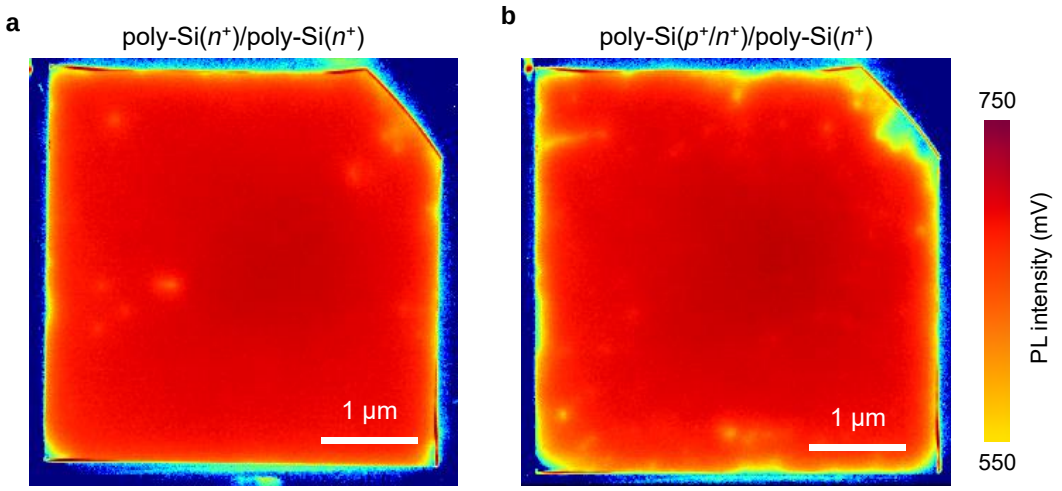

Supplementary Figure 13 | PL mappings of the related samples. PL images of samples with the structures of (**a**) poly-Si(n^+)/SiO_x/n-Si/SiO_x/poly-Si(n^+), and (**b**) poly-Si(p^+)/poly-Si(n^+)/SiO_x/n-Si/SiO_x/poly-Si(n^+).

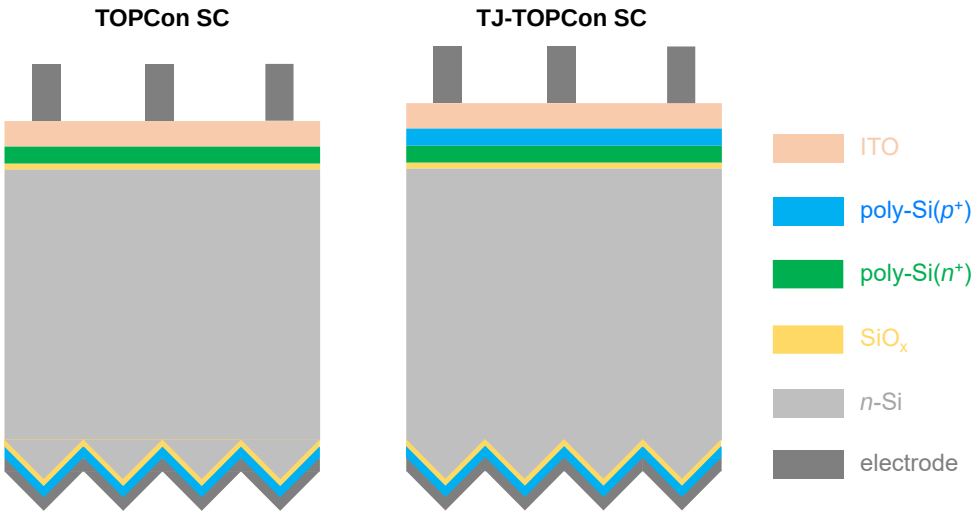

Supplementary Figure 14 | Structures of the related devices. Schematic diagrams of TOPCon and TJ-TOPCon SCs.

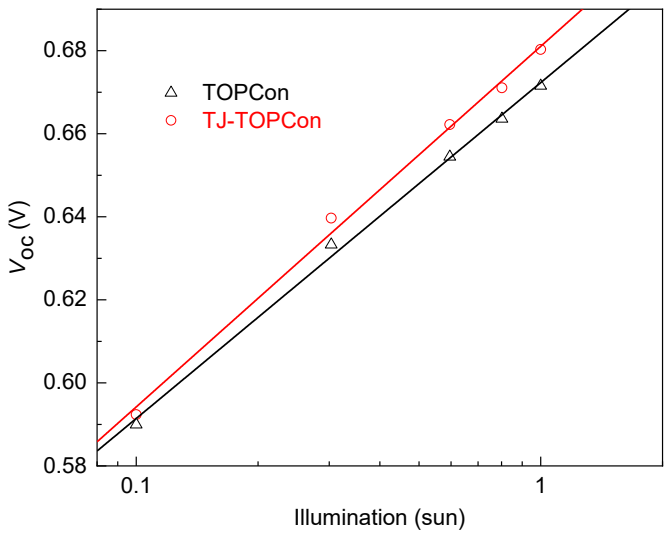

Supplementary Figure 15 | V_{oc} values under the various light intensity. Illumination-dependent V_{oc} for TOPCon and TJ-TOPCon SCs. Linear fitting was employed to fit the data depicted in these plots.

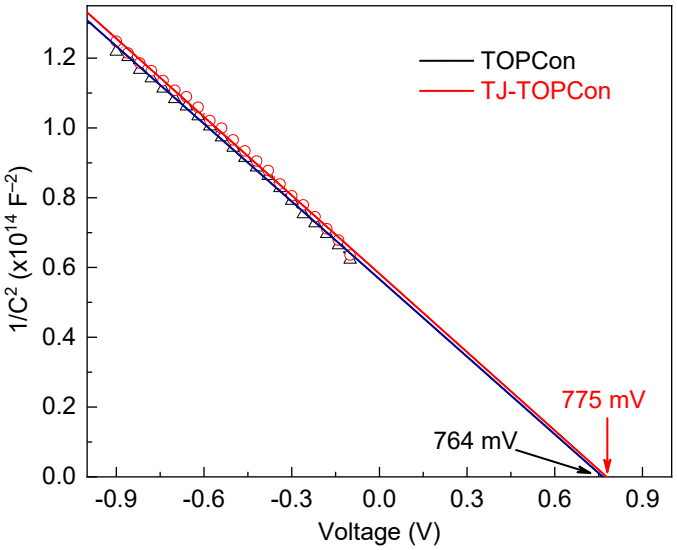

Supplementary Figure 16 | *C-V* measurements of the two related cases. Capacitance-voltage (*C-V*) curves for TOPCon and TJ-TOPCon SCs. The built-in voltage (V_{bi}) of these devices can be extracted from these plots, which were determined to be 764 and 775 mV for the TOPCon and TJ-TOPCon SCs, respectively. Linear fitting was employed to fit the data depicted in these plots.

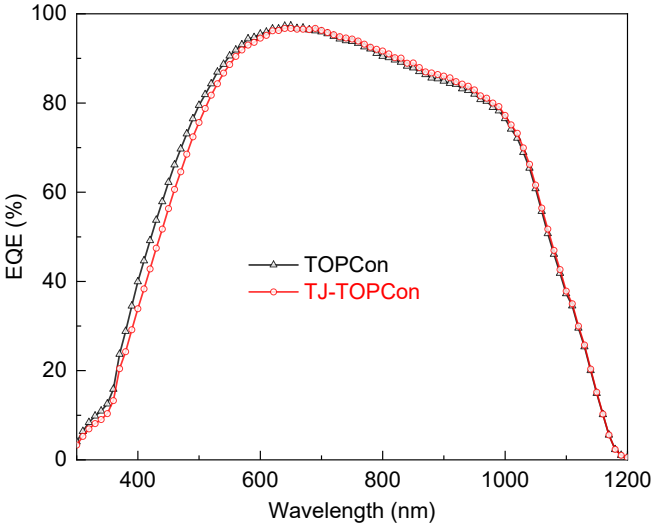

Supplementary Figure 17 | *EQE* spectra of the single-junction TOPCon SCs. *EQE* spectra of TOPCon and TJ-TOPCon SCs.

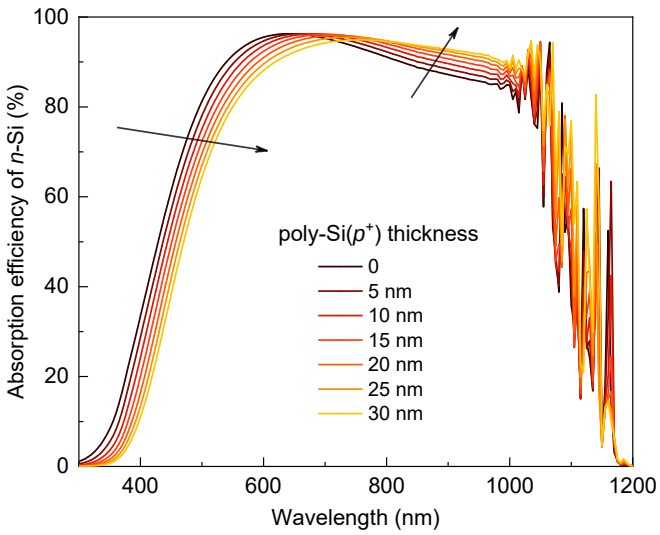

Supplementary Figure 18 | Absorption efficiency spectra. Simulated absorption efficiency spectra under the various poly-Si(p^+) thicknesses.

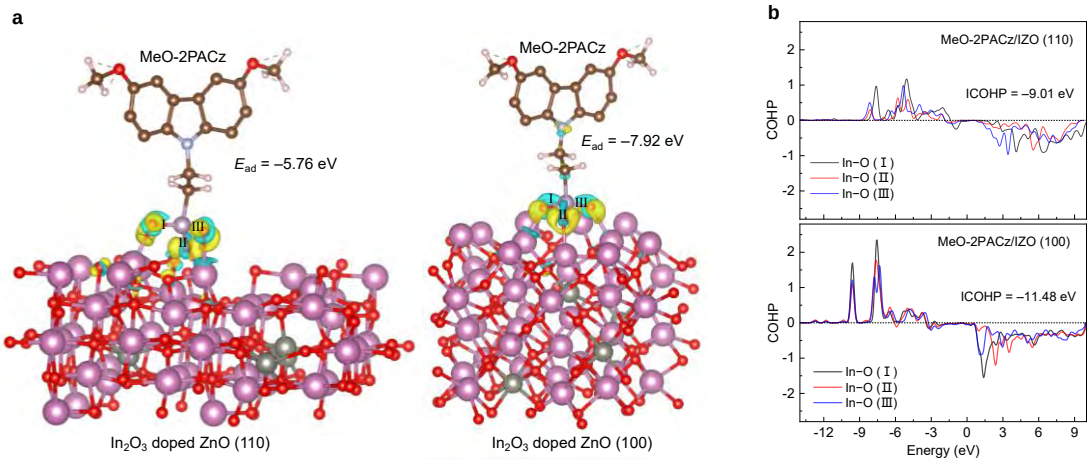

Supplementary Figure 19 | Local charge density distributions and the corresponding COHP curves. (**a**) Local charge density distributions of MeO-2PACz adsorbed IZO (110) and (100), and (**b**) the corresponding COHP curves. The cyan and yellow volumes correspond to electron-depleted or electron-enriched regions, respectively. The numerals I, II, and III indicate the number of bonds.

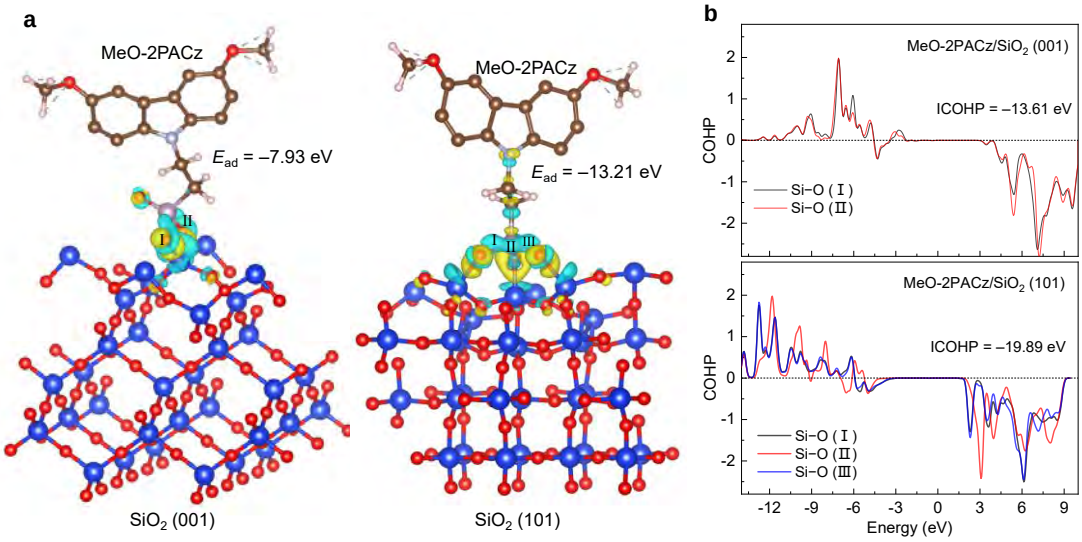

Supplementary Figure 20 | Local charge density distributions and the corresponding COHP curves. (**a**) Local charge density distributions of MeO-2PACz adsorbed SiO_2 (001) and (101), and (**b**) the corresponding COHP curves. The cyan and yellow volumes correspond to electron-depleted or electron-enriched regions, respectively. The numerals I, II, and III indicate the number of bonds.

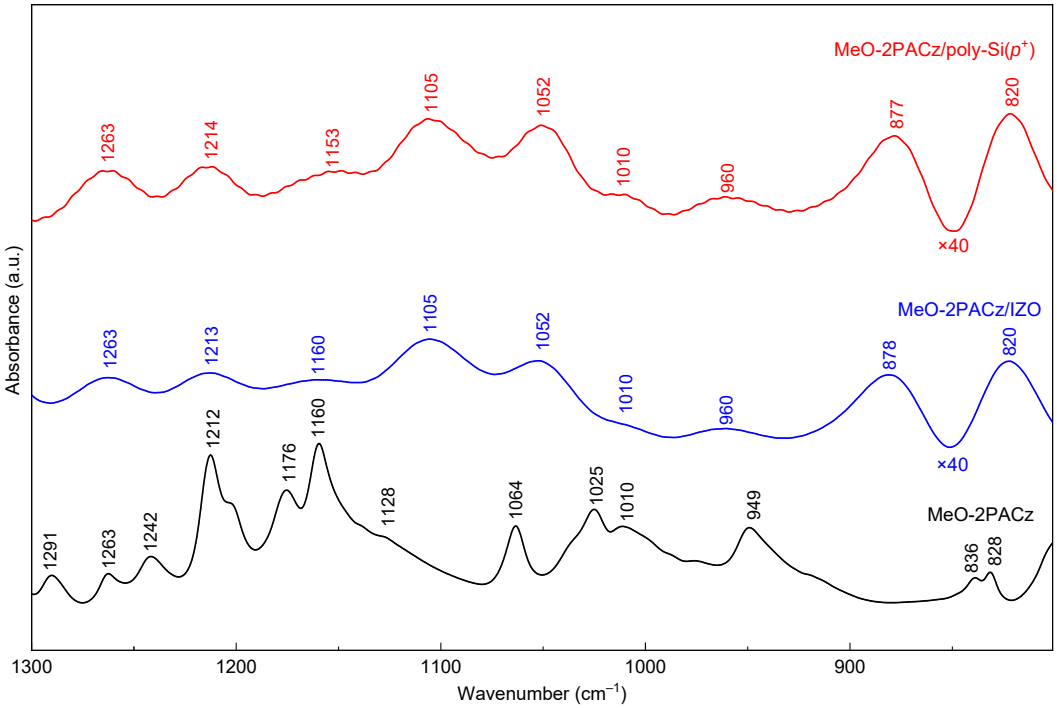

Supplementary Figure 21 | FTIR absorbance spectra. FTIR absorbance spectra of bulk MeO-2PACz (in KBr tablet), MeO-2PACz coated IZO, and poly-Si(p^+) samples, where the characteristic peaks were marked. In the considered spectrum range, the characteristic peaks of bulk MeO-2PACz include the carbazole stretching peaks (828, 836, and 949 cm^{-1}), the substituent stretching peak of carbazole (1010 cm^{-1}), and stretching peaks of P–OH (1025 cm^{-1}), C–C (1128 cm^{-1}), P=O (1160 cm^{-1}), C–N (1212 cm^{-1}) and C–O (1263 cm^{-1}). Among them, the carbazole stretching peaks at 828, 836, and 949 cm^{-1} were shifted to 820, 878, and 960 cm^{-1}, and C–C stretching peak at 1128 cm^{-1} was shifted to 1105 cm^{-1} for the MeO-2PACz coated IZO and poly-Si(p^+) samples, due to the differences in the flexibility of large groups or group chains in bulk materials and thin films. The P–OH stretching peak at 1025 cm^{-1} was shifted to 1052 cm^{-1}, which means that the P–OH bonds lose H and combine with the IZO and poly-Si(p^+) substrate to form P–O–Zn and P–O–Si, respectively. In addition, it is observed that the position of the P=O bond for the poly-Si(p^+) sample was shifted by 7 cm^{-1}, mainly meaning the different adsorption sites between IZO and poly-Si(p^+). The other absorption peaks at 1064, 1176, 1242, and 1291 cm^{-1} were the results of the movement of groups within or between chains, which can only be observed in the bulk MeO-2PACz but not in the MeO-2PACz coated IZO and poly-Si(p^+) samples.

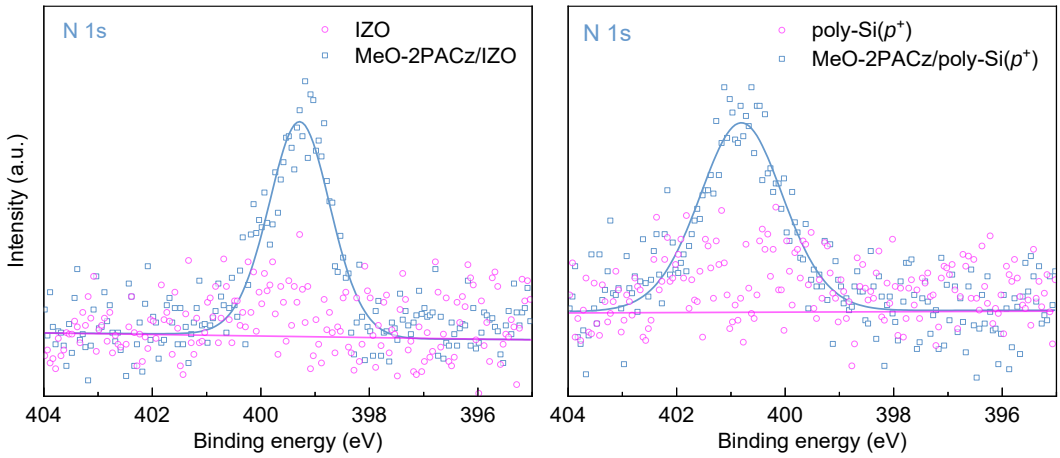

Supplementary Figure 22 | XPS spectra of N 1s for the related samples. XPS spectra of N 1s region of IZO and MeO-2PACz coated IZO samples, together with poly-Si(p^+) and MeO-2PACz coated poly-Si(p^+) samples. All plots were fitted using a Gaussian peak-fitting.

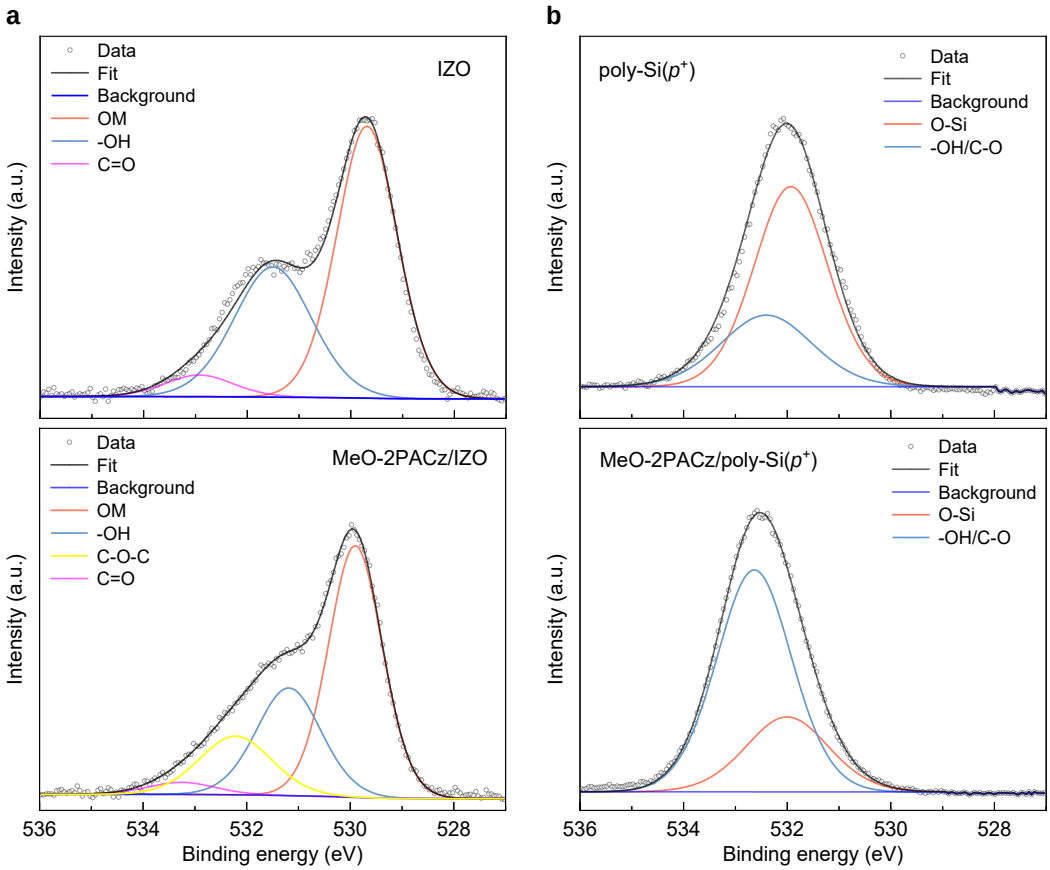

Supplementary Figure 23 | XPS spectra of O 1s for the related samples. XPS spectra of O 1s region of (**a**) IZO and MeO-2PACz coated IZO, and (**b**) poly-Si(p^+) and MeO-2PACz coated poly-Si(p^+) samples. All plots were fitted using a Gaussian peak-fitting.

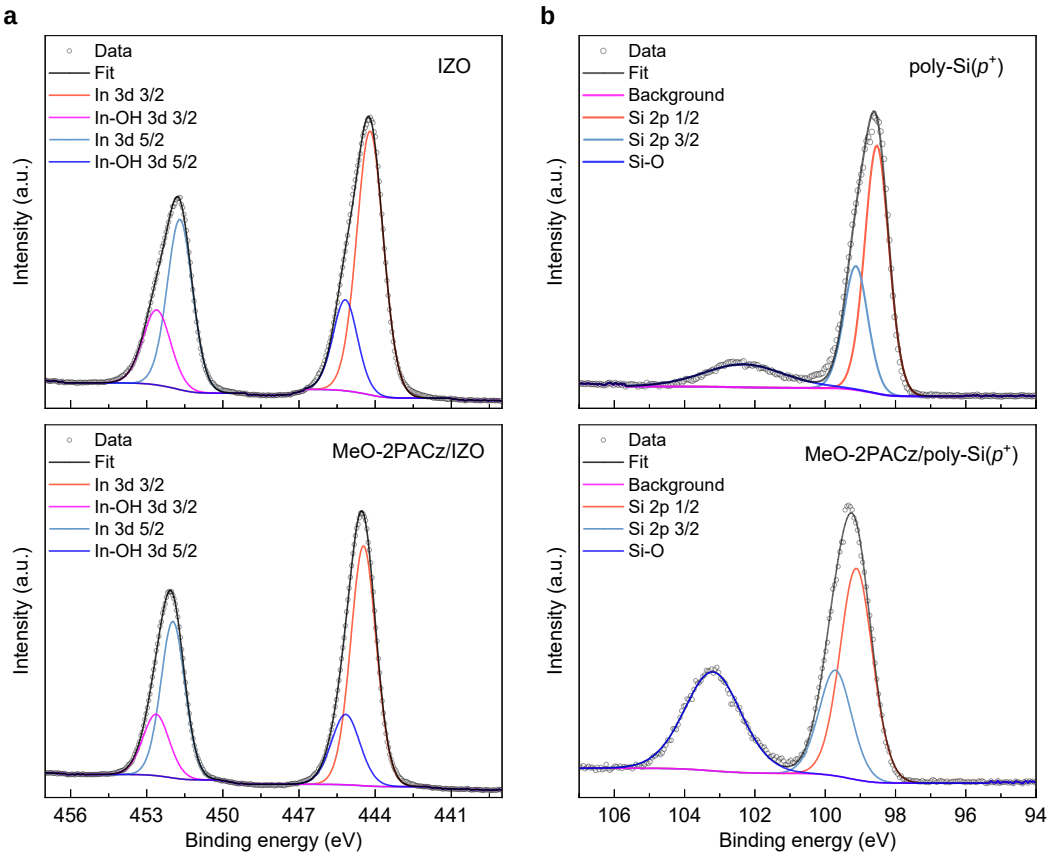

Supplementary Figure 24 | XPS spectra of In 3d and Si 2p for the related samples. XPS spectra of In 3d and Si 2p regions of (**a**) IZO and MeO-2PACz coated IZO, and (**b**) poly-Si(p^+) and MeO-2PACz coated poly-Si(p^+) samples. All plots were fitted using a Gaussian peak-fitting.

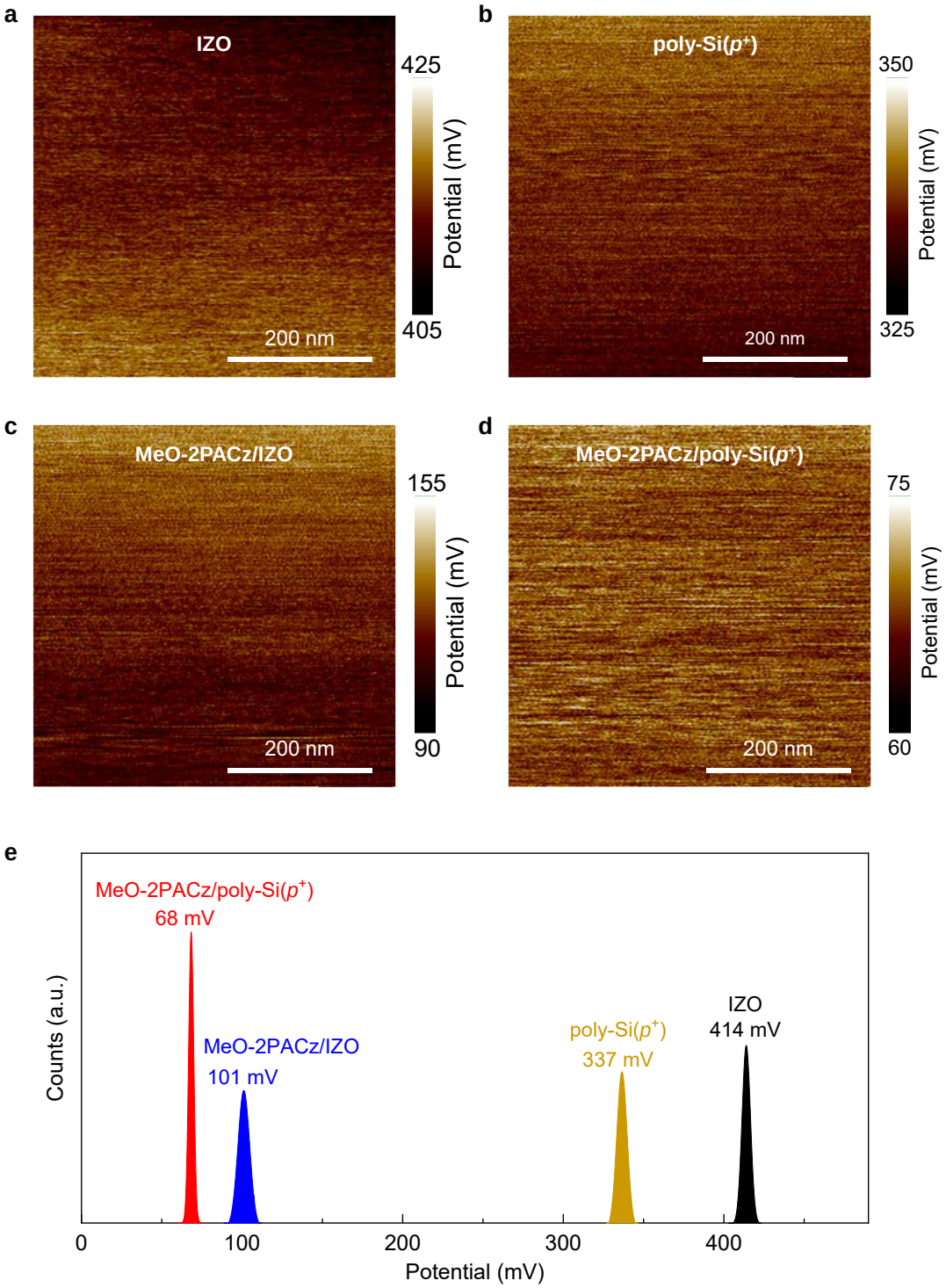

Supplementary Figure 25 | KPFM measurements of the different samples. 2D KPFM maps of the (**a**) IZO, (**b**) poly-Si(p^+), (**c**) MeO-2PACz coated IZO, and (**d**) MeO-2PACz coated poly-Si(p^+) samples, and (**e**) the corresponding potential distributions.

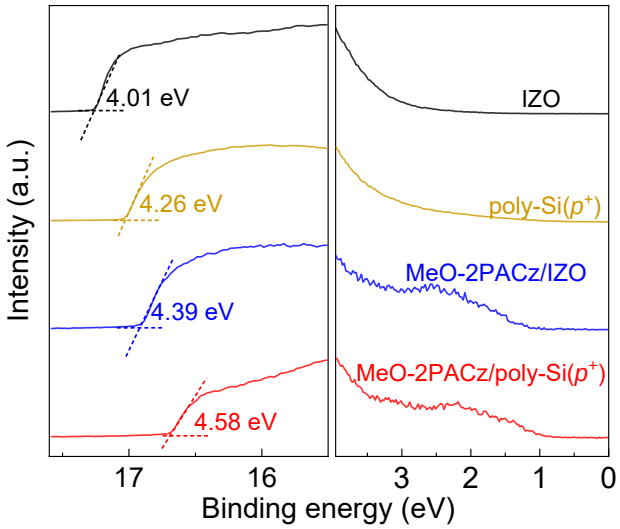

Supplementary Figure 26 | UPS measurements of the related samples. Retested UPS spectra of four related samples, *i.e.*, IZO, poly-Si(p^+), MeO-2PACz/IZO, and MeO-2PACz/poly-Si(p^+).

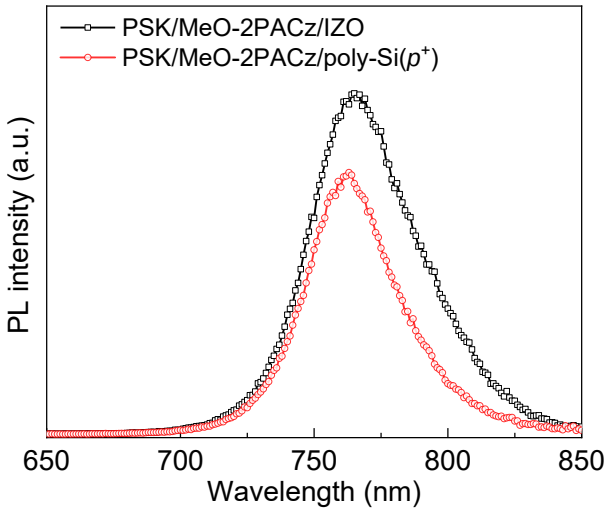

Supplementary Figure 27 | Steady-state PL measurements of the related samples. Retested steady-state PL spectra of two related samples.

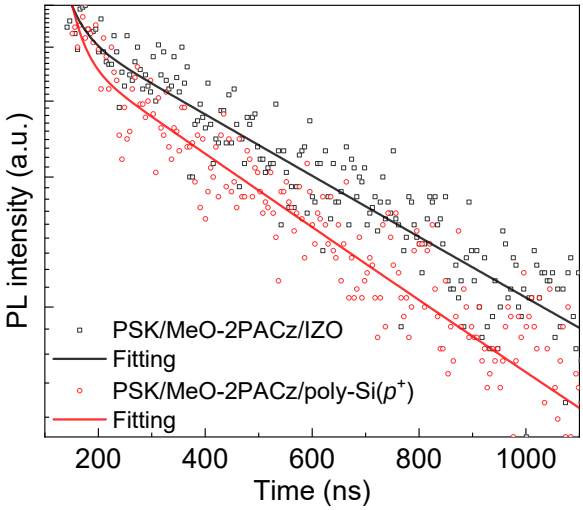

Supplementary Figure 28 | tr-PL measurements of the related samples. Retested time-resolved PL spectra of two related samples. A bi-exponential function was employed to fit these plots.

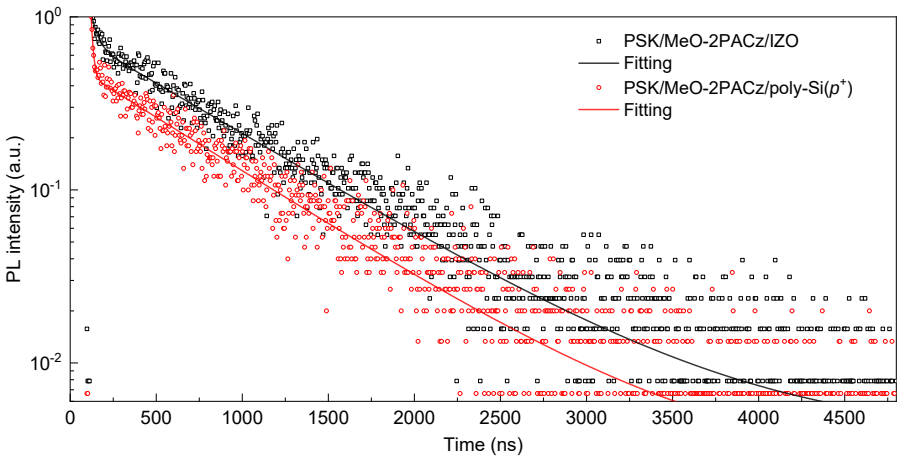

Supplementary Figure 29 | Prolonged tr-PL curves of the related samples. Prolonged time-resolved PL spectra of perovskite films deposited on MeO-2PACz/IZO and MeO-2PACz/poly-Si(p^+) substrates. A bi-exponential function was employed to fit these plots.

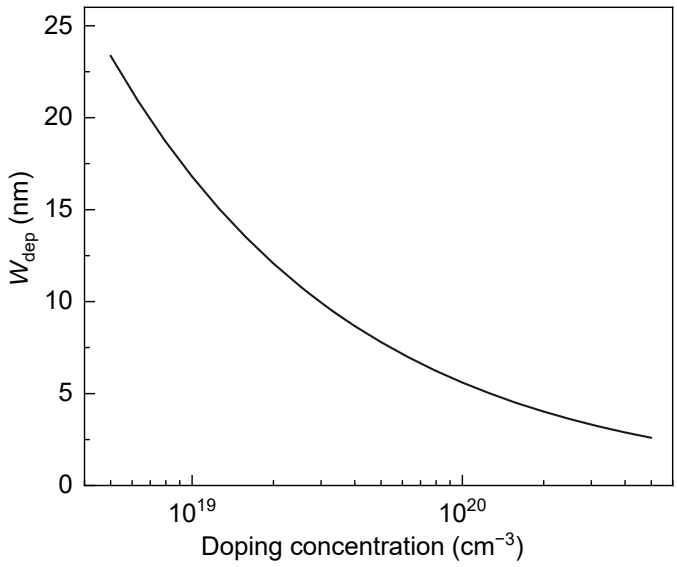

Supplementary Figure 30 | Simulated depletion width. Simulated depletion width (W_{dep}) as a function of the doping concentration of poly-Si, calculated by the equation: $W_{\mathrm{dep}} = [\frac{2\varepsilon_0\varepsilon_s}{q}\left(\frac{N_a+N_d}{N_aN_d}\right)V_D]^{0.5}$.

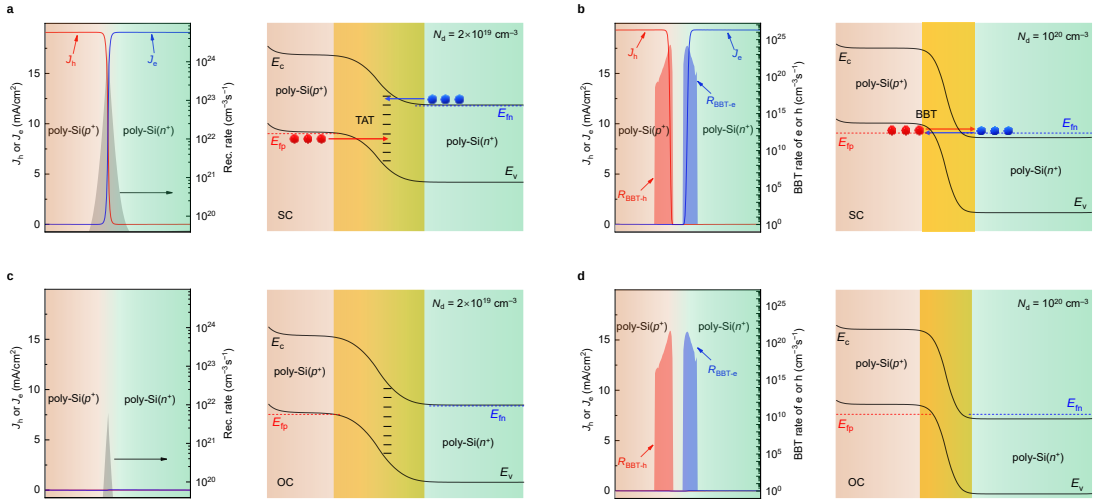

Supplementary Figure 31 | Simulated current and recombination distributions. J_h and J_e distributions, Rec./BBT rates, and the corresponding energy diagrams within poly-Si(p^+) and poly-Si(n^+) regions at (**a**)/(**b**) SC condition with $N_d = 10^{19}/10^{20}$ cm^{-3}, and (**c**)/(**d**) OC condition with $N_d = 2\times10^{19}/10^{20}$ cm^{-3}.

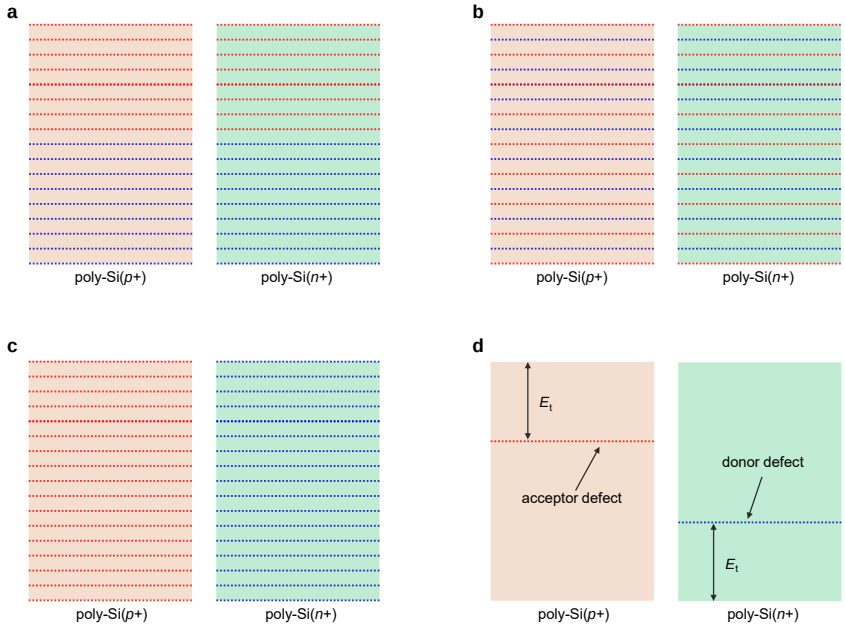

Supplementary Figure 32 | Defect types used for simulation. Sketch maps of four types of defects used for this simulation, *i.e.*, (**a**) defect I: acceptor-/donor-type defects distributed upon/below the middle bandgap of poly-Si for both poly-Si(p^+) and poly-Si(n^+), (**b**) defect II: acceptor- and donor-type defects distributed within the whole bandgap of poly-Si for both poly-Si(p^+) and poly-Si(n^+), (**c**) defect III: acceptor- and donor-type defects distributed within the whole bandgap of poly-Si for poly-Si(p^+) and poly-Si(n^+), respectively, and (**d**) defect IV: single-level defects with the accepter/donor energy level of E_t from conduction/valence band of poly-Si.

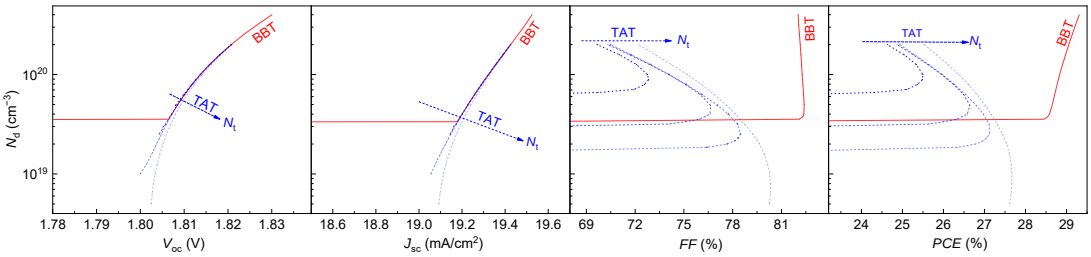

Supplementary Figure 33 | Performance of TSCs under the defect II. Electrical parameters (*i.e.*, V_{oc}, J_{sc}, *FF,* and *PCE*) as a function of N_d of poly-Si(p^+) and poly-Si(n^+), where defect II, *i.e.*, acceptor-type and donor-type defects distributed within the whole bandgap of poly-Si for both poly-Si(p^+) and poly-Si(n^+), is used for simulation.

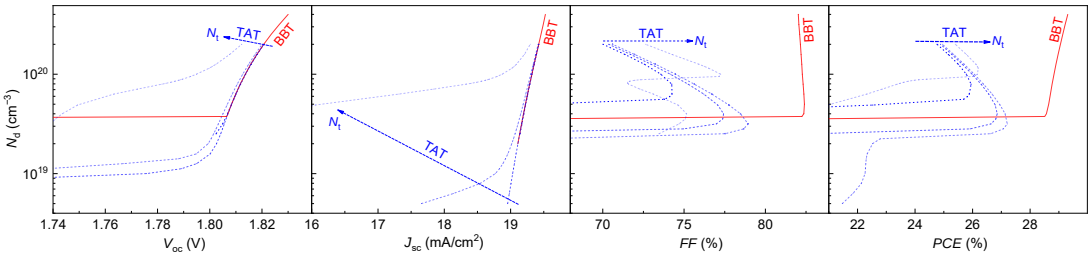

Supplementary Figure 34 | Performance of TSCs under the defect III. Electrical parameters (*i.e.*, V_{oc}, J_{sc}, *FF,* and *PCE*) as a function of N_d of poly-Si(p^+) and poly-Si(n^+), where defect III: *i.e.*, acceptor- and donor-type defects distributed within the whole bandgap of poly-Si for poly-Si(p^+) and poly-Si(n^+), respectively, is used for simulation.

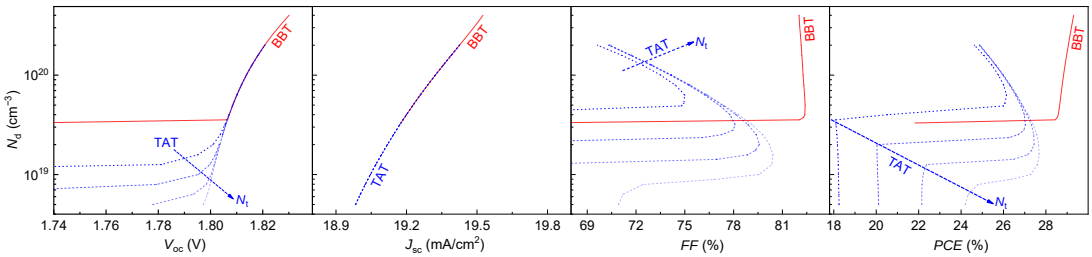

Supplementary Figure 35 | Performance of TSCs under the defect IV. Electrical parameters (*i.e.*, V_{oc}, J_{sc}, *FF,* and *PCE*) as a function of N_d of poly-Si(p^+) and poly-Si(n^+), where defect IV, *i.e.*, single-level defect, is used for simulation.

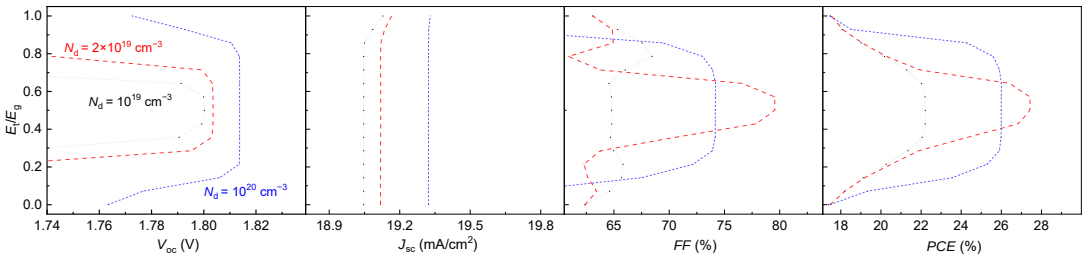

Supplementary Figure 36 | Performance of TSCs under the single-level defect. Electrical parameters (*i.e.*, V_{oc}, J_{sc}, *FF,* and *PCE*) as a function of E_t/E_g under $N_d = 10^{19}$, 2×10^{19}, and 10^{20} cm^{-3}.

Supplementary Note 1. Extraction of passivation properties

The detailed information on the extraction of the passivation qualities (*i.e.*, iV_{oc} and τ_{eff}) from Sinton equipment is demonstrated. For the passivation measurement, double-sided symmetrical structures were used. For a given excess minority carrier charge concentration (Δn) determined by QSSPC measurement, iV_{oc} can be calculated by:

$$iV_{oc} = \frac{kT}{q} In[\frac{\Delta n(N_d+\Delta n)}{n_i^2}] \quad \text{(S1)}$$

where N_d is the donor doping concentration of the Si substrates, n_i is the intrinsic carrier concentration of Si, and Δn is the excess minority carrier concentration at the boundary of the space charge region. The effective lifetime, τ_{eff}, defined by the specific recombination species including the recombination within the bulk and at the surfaces, can be described by:

$$\frac{1}{\tau_{eff}} = \frac{1}{\tau_b} + (J_{0,front} + J_{0,rear})\frac{(N_d+\Delta n)}{qWn_i^2} \quad \text{(S2)}$$

where W is the thickness of the Si substrates, τ_b is the bulk lifetime of bulk Si, $J_{0,front}$ ($J_{0,rear}$) is the saturation current density from the front (rear) side of the Si surface, respectively.

Supplementary Note 2. Details of electrical simulation

In this study, the finite element method by coupling optical and electrical models was used. The optical simulation was carried out by solving Maxwell's equations to obtain the frequency-dependent and spatial-dependent electromagnetic distributions. In that case, the optical properties including optical absorption efficiency and optical generation rate can be thus obtained. Based on the optical results (*i.e.*, spatial-dependent photogeneration rate), the electrical simulation was then performed by addressing Poisson's equation and carrier transport equations as follows:

$$-\nabla \cdot (\varepsilon_{\mathrm{r}} \nabla V) = q(p - n + N_{\mathrm{d}} - N_{\mathrm{a}} + n_{\mathrm{t}}^{+} - n_{\mathrm{t}}^{-}) \tag{S3}$$

$$\frac{\partial n}{\partial t} = \frac{1}{q}\nabla \cdot J_n + G - R;\ \frac{\partial p}{\partial t} = -\frac{1}{q}\nabla \cdot J_p + G - R \tag{S4}$$

$$J_n = qn\mu_n\varepsilon + qD_n\nabla n;\ J_p = qp\mu_p\varepsilon + qD_p\nabla p \tag{S5}$$

where ε_{r} is the dielectric constant, V is the electrostatic potential, n/p is the electron/hole concentration, $N_{\mathrm{d}}/N_{\mathrm{a}}$ is donor/acceptor concentration, $n_{\mathrm{t}}^{+}/n_{\mathrm{t}}^{-}$ is the ionized donor/acceptor trap density, J_n/J_p is the electron/hole current density, μ_n/μ_p is the electron/hole mobility, D_n/D_p is the electron/hole diffusion coefficient, which can be estimated by Einstein's relation, *i.e.*, $D_{n/p} = \mu_{n/p}k_{\mathrm{B}}T/q$ with k_{B} of Boltzmann's constant and T of the temperature (which was set to be 300 K in this simulation), ε is the electric field, which can be calculated by $\varepsilon = -\nabla V$, and $\partial n/\partial t$ ($\partial p/\partial t$) is the transient electron (hole) concentration change (which was set to be 0 for the steady state), G is the carrier generation ratio obtained from optical simulation. R is the total carrier recombination rate, which can be described by four contributions, *i.e.*, radiative or direct recombination rate, R_{rad}, Auger recombination rate, R_{Aug}, Shockley-Read-Hall recombination rate, R_{SRH}, and surface recombination rate, R_{sur}, as follows:

$$R = R_{\mathrm{rad}} + R_{\mathrm{Aug}} + R_{\mathrm{SRH}} + R_{\mathrm{sur}} \tag{S6}$$

$$R_{\mathrm{rad}} = B_{\mathrm{rad}}(np - n_i^2) \tag{S7}$$

$$R_{\mathrm{Aug}} = (A_n n + A_p p)(np - n_i^2) \tag{S8}$$

$$R_{\mathrm{SRH}} = \frac{np - n_i^2}{\tau_p(n + n_t) + \tau_n(p + p_t)} \tag{S9}$$

$$R_{\mathrm{sur}} = \frac{np - n_i^2}{(n + n_{ts})/S_n + (p + p_{ts})/S_p} \tag{S10}$$

where B_{rad} is the radiative recombination coefficient, A_n/A_p is the electron/hole Auger recombination coefficient, τ_n/τ_p is the electron/hole lifetime, S_n/S_p is the surface recombination velocity of the electrons/holes, n_i is the intrinsic carrier concentration, n_t/p_t is the bulk electron/hole concentration of the trap states, and n_{ts}/p_{ts} is the corresponding trap density at surfaces.

For SiO_x tunneling, a direct quantum tunneling model was used. By taking into

account carrier statistics and integrating over lateral energy, the tunneling current can be expressed:

$$J = \frac{qkTm_{\text{eff}}}{2\pi^2 h^3} \int T(E)\, ln \left\{ \frac{1+\exp\left[\frac{E_{Fr}-E}{kT}\right]}{1+\exp\left[\frac{E_{Fl}-E}{kT}\right]} \right\} dE \tag{S11}$$

where m_{eff} is the effective mass, E_{fl} and E_{fr} are the quasi-Fermi levels on either side of the barrier. The transmission probability, $T(E)$, of an electron or hole through the potential barrier can be calculated using Wentzel-Kramers-Brillouin (WKB) approximation.

Trap-Assisted Tunneling (TAT) models the trap-to-band phonon-assisted tunneling effects for Dirac wells, *i.e.*, tunneling of electrons from the valence band to the conduction band through trap or defect states. By modeling appropriate enhancement factors (*i.e.*, Γ_n^{DIRAC} and Γ_p^{DIRAC}), the lifetimes of holes and electrons can be modified so that the TAT effect can be calculated. For donor-like traps, the recombination term for traps becomes:

$$R_D = \frac{pn - n_i^2}{\frac{\tau_n}{1+\Gamma_n^{DIRAC}}\left[p + \text{DEGEN.FAC}\, n_i\, exp\left(\frac{E_i - E_t}{kT_L}\right)\right] + \frac{\tau_p}{1+\Gamma_n^{DIRAC}}\left[n + \frac{1}{\text{DEGEN.FAC}}\, n_i\, exp\left(\frac{E_t - E_i}{kT_L}\right)\right]} \tag{S12}$$

For acceptor like traps, the recombination term becomes:

$$R_A = \frac{pn - n_i^2}{\frac{\tau_n}{1+\Gamma_n^{DIRAC}}\left[p + \frac{1}{\text{DEGEN.FAC}}\, n_i\, exp\left(\frac{E_i - E_t}{kT_L}\right)\right] + \frac{\tau_p}{1+\Gamma_p^{DIRAC}}\left[n + \text{DEGEN.FAC}\, n_i\, exp\left(\frac{E_t - E_i}{kT_L}\right)\right]} \tag{S13}$$

where DEGEN.FAC is the degeneracy factor of the trap center, T_L is the lattice temperature, E_i is the intrinsic Fermi level position, E_t is the trap energy level. The field-effect enhancement term for electrons is expressed by:

$$\Gamma_n^{DIRAC} = \frac{\Delta En}{kT_L} \int_0^1 \exp\left(\frac{\Delta En}{kT_L} u - K_n u^{3/2}\right) du \tag{S14}$$

while the field-effect enhancement term for holes can be written as:

$$\Gamma_p^{DIRAC} = \frac{\Delta Ep}{kT_L} \int_0^1 \exp\left(\frac{\Delta En}{kT_L} u - K_p u^{3/2}\right) du \tag{S15}$$

where u is the integration variable, $\Delta E_n/\Delta E_p$ is the energy range where tunneling can occur for electrons/holes, and K_n and K_p are defined as:

$$K_n = \frac{4}{3} \frac{\sqrt{2m_0 m\_\text{tun} \Delta E_n^{\,3}}}{qh|E|} \tag{S16}$$

$$K_p = \frac{4}{3} \frac{\sqrt{2m_0 m\_\text{tun} \Delta E_n^{\,3}}}{qh|E|} \tag{S17}$$

h is the reduced Planck's constant, m_0 is the rest mass of an electron, and m_tun is the effective mass.

If a sufficiently high electric field exists within a device, local band bending may be sufficient to allow electrons to tunnel, by internal field emission, from the valence band into the conduction band. An additional electron is therefore generated in the conduction band and a hole in the valence band. This generation mechanism is implemented into the continuity equations. The tunneling generation rate, G_{BBT}, can be expressed as:

$$G_{\mathrm{BBT}} = D\ \mathrm{BB.A}\ E^{\mathrm{BB.GAMMA}} exp\ (-\frac{\mathrm{BB.B}}{E}) \tag{S18}$$

D is a statistical factor, and BB.A, BB.B, and BB.GAMMA are the parameters, which can be calculated according to:

$$\mathrm{BB.A} = \frac{q^2\sqrt{(2\times m\_\mathrm{tun}\ m_0)}\mathrm{BB.B}}{h^2\sqrt{E_{\mathrm{g}}}} \tag{S19}$$

$$\mathrm{BB.B} = \frac{\pi^2\ E_{\mathrm{g}}^{\frac{3}{2}}\sqrt{\frac{m\_\mathrm{tun}\ m_0}{2}}}{qh} \tag{S20}$$

and BB.GAMMA was fixed at 2 in this study.

Supplementary Table 1 | A summary of perovskite/c-Si tandem solar cells with interlayer-free design or various TRLs.

Year	Institution	Type	Top cell	Rear cell	Tunneling design	Area (cm^2)	V_{oc} (V)	*FF* (%)	J_{sc} (mA/cm^2)	*PCE* (%)	Ref
2015.03	MIT	n-i-p	Spiro/ $CH_3NH_3PbI_3/TiO_2$	Homojunction	n^{++}/p^{++} Si	1	1.58	75	11.5	13.7	1
2017.10	EPFL	n-i-p	Spiro/ $Cs_{0.19}MA_{0.81}PbI_3/C_{60}$	SHJ	nc-Si:H(n^+)/nc-Si:H(p^+)	0.25	1.751	77.5	16.8	22.8	2
						1.43	1.777	74.4	16.5	21.8	
						12.96	1.769	65.4	16.5	19.1	
2018.06	UNSW	n-i-p	Spiro/ $CH_3NH_3PbI_3/SnO_2$	Homojunction	none	4	1.68	78	16.1	21.0	3
						16	1.658	68	15.6	17.6	
2018.08	UNSW	n-i-p	Spiro/ $(FAPbI_3)_{0.83}(MAPbBr_3)_{0.17}/SnO_2$	Homojunction	none	16	1.740	78	16.2	21.8	4
2018.09	EPFL	p-i-n	$SnO_2/C_{60}/LiF/Cs_xFA_{1-x}Pb(I,Br)_3$/Spiro-TTB	SHJ	nc-Si:H(p^+)/nc-Si:H(n^+)	1.42	1.788	73.1	19.5	25.24	5
2018.12	ANU	n-i-p	Spiro or PTAA /$Cs_{0.05}Rb_{0.05}FA_{0.765}MA_{0.135}PbI_{2.55}Br_{0.45}/TiO_2$	Homojunction	none	/	1.7	78	17.2	22.9	6
				SHJ			1.76	78	17.8	24.1	
2019.03	EPFL	p-i-n	SnO_2/C_{60}/LiF/perovskite /Spiro-TTB	TOPCon	nc-Si:H(p^+)/nc-SiC_x(n^+)	1.42	1.741	74.7	19.5	25.41	7
2019.10	UNSW	n-i-p	Spiro/perovskite/SnO_2	Homojunction	none	4	1.732	81	16.5	23.1	8
2020.07	UWM	n-i-p	Spiro/$(FAPbI_3)_{0.83}(MAPbBr_3)_{0.17}/SnO_2$	Homojunction	none	1	1.68	80.2	15.8	21.3	9
2020.09	KAUST	p-i-n	SnO_2/C_{60}/FACsMAPb $I_{3-x}Br_x$/Spiro-TTB	SHJ	nc-Si:H(p^+)/nc-Si:H(n^+)	0.832	1.735	73.1	19.8	25.1	10
2021.05	BJUT	p-i-n	SnO_2/C_{60}/LiF/perovskite /Spiro-TTB	SHJ	μc-Si(p^+) /μc-n-SiO_x	1.2	1.74	76.73	19.44	25.9	11
2021.11	NKU	p-i-n	SnO_2/C_{60}/LiF/$FA_{0.9}Cs_{0.1}PbI_{2.87}Br_{0.13}$/Spiro-TTB	SHJ	nc-Si:H(p^+)/nc-Si:H(n^+)	0.509	1.808	76.85	19.78	27.48	12
2021.11	KU	n-i-p	MoO_x/spiro-OMeTAD/$Cs_{0.05}FA_{0.8}MA_{0.15}PbI_{2.55}Br_{0.45}/SnO_2$	TOPCon	none	0.1	1.527	67	16.6	16.9	14
2022.02	HZB	p-i-n	SnO_2/C_{60}/LiF/perovskite /2PACz	TOPCon	ITO/poly-Si(n^+)	1	1.8	69.25	17.07	21.34	15
2022.05	ANU/Jinko	p-i-n	SnO_2/C_{60}/perovskite /polyTPD/NiO_x	TOPCon	ITO/poly-Si(n^+)	1	1.794	78.27	19.68	27.63	16
2022.10	NIMTE	p-i-n	BCP:Ag/C_{60}/perovskite /NiO_x-NPs/Spiro-TTB	TOPCon	ITO/BCP:Ag/poly-Si(n^+)	0.1	1.73	80.31	18.78	26.06	17

2022.10	NKU	p-i-n	SnO_2/C_{60}/TEABr /perovskite/Spiro-TTB	SHJ	nc-Si:H(p^+)/nc-Si:H(n^+)	0.504	1.849	79.62	19.35	28.51	[13]
2022.11	NIMTE	p-i-n	BCP:Ag/C_{60}/perovskite /IZO/MeO-2PACz	TOPCon	IZO/poly-Si(n^+)	0.1	1.732	81	16.5	28.5	[18]
2023.01	NIMTE	p-i-n	BCP:Ag/C_{60}/perovskite /IZO/MeO-2PACz	TOPCon	IZO/poly-Si(n^+)	0.1 1	1.799 1.765	81.64 79.51	19.4 18.58	28.49 26.08	[19]
2023.03	Delft	p-i-n	SnO_2/C_{60}/choline chloride /perovskite/2PACz/NiO_x	TOPCon	ITO/poly-Si(n^+)	0.832	1.735	73.1	19.8	23.18	[20]
2023.07	NIMTE	p-i-n	BCP:Ag/C_{60}/perovskite /IZO/MeO-2PACz	TOPCon	poly-Si(p^+)/poly-Si(n^+)	0.1	1.83	81.02	19.71	29.22	This work

Supplementary Table 2 | Passivation parameters of the different samples.

Samples	iV_{oc} (mV) @ 1 sun	τ_{eff} (ms) @ 1× 10^{16} cm^{-3}	J_0 (fA/cm^2) @ 1× 10^{15} cm^{-3}
poly-Si(n^+)/SiO_x/n-Si/SiO_x/poly-Si(n^+)	735	10.21	2.95
poly-Si(p^+)/poly-Si(n^+)/SiO_x/n-Si/SiO_x/poly-Si(n^+)	736	10.54	2.14
poly-Si(n^+)/SiO_x/n-Si/SiO_x/poly-Si(p^+)	690	0.47	75.50
poly-Si(p^+)/poly-Si(n^+)/SiO_x/n-Si/SiO_x/poly-Si(p^+)	690	0.50	75.30

Supplementary Table 3 | ICOHP of the different cases.

Samples	E_{ad} (eV)	ICOHP(I) (eV)	ICOHP(II) (eV)	ICOHP(III) (eV)	ICOHP(tot) (eV)
IZO (110)	–5.8	–3.61	–2.21	–3.19	–9.0
IZO (111)	–6.6	–3.48	–3.47	–3.44	–10.4
IZO (100)	–7.9	–4.18	–3.83	–3.47	–11.5
SiO_2 (001)	–6.8	–7.93	–6.77	/	–13.6
SiO_2 (111)	–11.9	–6.50	–5.94	–6.00	–18.4
SiO_2 (101)	–13.2	–6.46	–6.94	–6.48	–19.9

Supplementary Table 4 | Element contents of the different samples.

Samples	Zn	In	Si	O	C	P	N
IZO	3.15	25.56	/	41.76	29.53	/	/
MeO-2PACz/IZO	1.29	21.30	/	37.68	38.20	0.79	0.74
poly-Si(p^+)	/	/	56.27	26.54	17.18	/	/
MeO-2PACz/poly-Si(p^+)	/	/	32.47	36.29	26.20	2.80	2.24

Supplementary Table 5 | The time-resolved photoluminescence (trPL) fitting parameters are estimated by the bi-exponential decay equation $y = y_0 + A1\exp(-x/\tau_1) + A2\exp(-x/\tau_2)$. The average lifetime ($\tau_{ave}$) was obtained from $\tau_{ave} = (A1\tau_1^2 + A2\tau_2^2)/(A1\tau_1 + A2\tau_2)$.

Samples		A1	τ_1 (ns)	A2	τ_2 (ns)	τ_{ave} (ns)
Group 1	PSK/MeO-2PACz/IZO	46.0	36.2	87.1	737.4	719.7
	PSK/MeO-2PACz/poly-Si(p^+)	123.4	12.1	67.9	692.9	672.0
Group 2	PSK/MeO-2PACz/IZO	41.7	29.3	87.7	604.9	591.9
	PSK/MeO-2PACz/poly-Si(p^+)	103.1	24.8	78.5	503.7	474.6

Supplementary Table 6 | Lattice parameters for the bulk In_2O_3, SiO_2, and Si, respectively.

Samples	space group	a (Å)	b (Å)	c (Å)	α	β	γ
In_2O_3	I213	10.12	10.12	10.12	90°	90°	90°
SiO_2	FD-3M	7.16	7.16	7.16	90°	90°	90°
Si	FD-3M	5.43	5.43	5.43	90°	90°	90°

Supplementary Table 7 | Parameters used for electrical simulations.

Material parameters	C60	Perovskite	MeO-2PACz	poly-Si(p^+)	poly-Si(n^+)	c-Si
Thickness, nm	20	450	2	15	15	1.8×10^5
Electron affinity, χ (eV)	3.9	3.9	2.16	4.05	4.05	4.05
Bandgap energy, E_g (eV)	3.5	1.65	3.18	doping dep.	doping dep.	1.12
Relative dielectric permittivity, ε_r	3.9	6.5	3.5	11.7	11.7	11.7
Effective conduction band density, N_c (cm^{-3})	2.2×10^{18}	2.2×10^{18}	10^{21}	2.8×10^{19}	2.8×10^{19}	2.8×10^{19}
Effective valence band density, N_v (cm^{-3})	1.8×10^{19}	1.8×10^{19}	10^{21}	1.04×10^{19}	1.04×10^{19}	1.04×10^{19}
Donor doping concentration, N_d (cm^{-3})	5×10^{19}	/	/	various	/	1.04×10^{15}
Acceptor doping concentration, N_a (cm^{-3})	/	/	1×10^{18}	/	various	/
Mobility of electron/hole, μ_n/μ_p (cm^2/Vs)	$1\times10^{-3}/1\times10^{-3}$	10/10	0.001/0.001	doping dep.	doping dep.	1000/800
SRH life time, τ_n/τ_p (s)	$1\times10^{-6}/1\times10^{-6}$/	/	$1\times10^{-5}/1\times10^{-6}$	doping dep.	doping dep.	10^4
Radiative recombination coefficient, C_{Rad} (cm^3s^{-1})	/	5×10^{-11}	/	9.5×10^{-15}	9.5×10^{-15}	9.5×10^{-15}
Auger recombination coefficient, A_n/A_p (cm^6s^{-1})	/	2.3×10^{-29}	/	$2.8/0.99\times10^{-31}$	$2.8/0.99\times10^{-31}$	$2.8/0.99\times10^{-31}$

Supplementary References

1. Mailoa, J. P. *et al.* A 2-terminal perovskite/silicon multijunction solar cell enabled by a silicon tunnel junction. *Appl. Phys. Lett.* **106**, 121105 (2015).
2. Sahli, F. *et al.* Improved optics in monolithic perovskite/silicon tandem solar cells with a nanocrystalline silicon recombination junction. *Adv. Energy Mater.* **8**, 1701609 (2017).
3. Zheng, J. *et al.* Large area efficient interface layer free monolithic perovskite/homo-junction-silicon tandem solar cell with over 20% efficiency. *Energy Environ. Sci.* **11**, 2432–2443 (2018).
4. Zheng, J. *et al*. 21.8% Efficient Monolithic Perovskite/Homo-Junction-Silicon Tandem Solar Cell on 16 cm^2. *ACS Energy Lett.* **3,** 2299–2300 (2018).
5. Sahli, F. *et al.* Fully textured monolithic perovskite/silicon tandem solar cells with 25.2% power conversion efficiency. *Nat. Mater.* **17**, 820–826 (2018).
6. Shen, H. *et al.* In situ recombination junction between p-Si and TiO_2 enables high-efficiency monolithic perovskite/Si tandem cells. *Sci. Adv.* **4**, eaau9711 (2018).
7. Nogay, G. *et al.* 25.1%-Efficient monolithic perovskite/silicon tandem solar cell based on a p-type monocrystalline textured silicon wafer and high-temperature passivating contacts. *ACS Energy Lett.* **4**, 844–845 (2019).
8. Zheng, J. *et al.* Large-area 23%-efficient monolithic perovskite/homojunction-silicon tandem solar cell with enhanced uv stability using down-shifting material. *ACS Energy Lett.* **4**, 2623–2631 (2019).
9. Li, W. *et al.* High-performance solar flow battery powered by a perovskite/silicon tandem solar cell. *Nat. Mater.* **19**, 1326–1331 (2021).
10. Aydin, E. *et al.* Interplay between temperature and bandgap energies on the outdoor performance of perovskite/silicon tandem solar cells. *Nat. Energy* 5, 851–859. (2020).
11. He, Y. *et al*. Minimizing open-circuit voltage loss in perovskite/Si tandem solar cells via exploring the synergic effect of cations and anions. *Phys. Status Solidi-R* **15**, 2100119 (2021)
12. Li, Y. *et al*. Wide bandgap interface layer induced stabilized perovskite/silicon tandem solar cells with stability over ten thousand hours. *Adv. Energy Mater.* **11**, 2102046 (2021).
13. Xu, Q. et al. Conductive passivator for efficient monolithic perovskite/silicon tandem solar cell on commercially textured silicon. *Adv. Energy Mater.* **12**, 2202404 (2022).
14. Hyun, J. et al. Efficient n-i-p monolithic perovskite/silicon tandem solar cells with tin oxide via a chemical bath deposition method. *Sol. RRL* **14**, 7614 (2021).
15. Mariotti, S. et al. Monolithic perovskite silicon tandem solar cells fabricated using industrial p-type polycrystalline silicon on oxide/passivated emitter and rear cell silicon bottom cell technology. *Energies* **6**, 2101066 (2022).
16. Wu, Y. et al. 27.6% Perovskite/c-Si tandem solar cells using industrial fabricated topcon device. *Adv. Energy Mater.* **12**, 2200821 (2022).
17. Ying, Z. et al. Bathocuproine:Ag complex functionalized tunneling junction for efficient monolithic perovskite/topcon silicon tandem solar cell. *Sol. RRL* **6**, 2200793 (2022).
18. Ying, Z. et al. Monolithic perovskite/black-silicon tandems based on tunnel oxide passivated contacts. *Joule* **6**, 2644–2661 (2022).
19. Zheng, J. et al. Balancing charge-carrier transport and recombination for perovskite/TOPCon tandem solar cells with double-textured structures. *Adv. Energy Mater.* **13**, 2203006 (2022).
20. Singh, M. *et al.* Crystalline silicon solar cells with thin poly-SiO_x carrierselective passivating contacts for perovskite/c-Si tandem applications. *Prog Photovolt Res Appl.* 3693 (2023).